J. Fluid Mech. (2024), *vol*. 1000, A40, doi:10.1017/jfm.2024.844

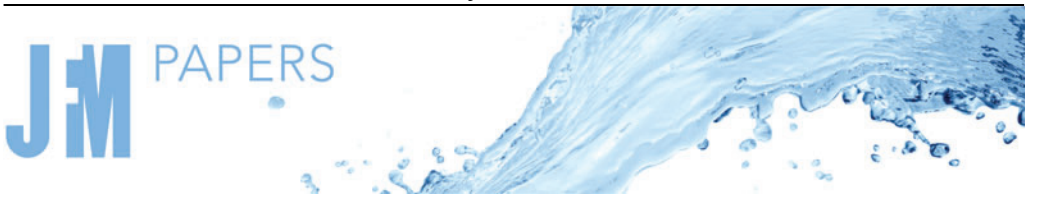

Transition to turbulence in rough plane Couette flow

S. Gokul[1] **and Vagesh D. Narasimhamurthy**[1],†

[1]Department of Applied Mechanics and Biomedical Engineering, Indian Institute of Technology Madras, Chennai 600036, India

(Received 16 October 2023; revised 21 July 2024; accepted 29 August 2024)

This DNS study considers transition to turbulence in plane Couette flow (pCf) with a rough stationary wall and a smooth moving wall. The roughness elements are square ribs of height $k = 0.2h$ (where h is the half-channel height). Two different pitch separations, $\lambda = 2k$ and $10k$, are considered, i.e. d-type and k-type roughness, respectively. The transition in both rough pCf cases takes place through a stage of alternate laminar–turbulent bands aligned in an oblique fashion. However, roughness causes a shift in the transitional Reynolds number (Re) range. In the k-type roughness, stable bands are observed in the range $Re \in [300, 325]$, which is a downwards shift from the transitional Re range for the smooth pCf ($Re \in [325, 400]$). The d-type roughness, on the other hand, surprisingly shifts the transitional Re range upwards to $Re \in [350, 425]$. This peculiar behaviour is associated with the ability of the ribs to shed and regenerate vorticity. Large-scale components extracted using a filtering process relate to the transition bands and flow parallel to the oblique laminar–turbulent boundaries. Counter-rotating vortices are present in the turbulent regions of the flow field, which exist in tandem with the high- and low-velocity streaks. Another interesting observation is the secondary Reynolds shear stresses, $-\overline{v'u'}$ and $-\overline{w'v'}$, which are non-zero in the transitional regime, in contrast to the turbulent regime where they are negligible.

Key words: turbulence simulation, turbulent transition, turbulent boundary layers

1. Introduction

In fluid mechanics, plane Couette flow (pCf) demonstrates the flow of a viscous fluid between two infinite parallel plates in relative motion. This shear-driven flow has attracted attention from researchers for many decades. It is distinct from other wall-bounded flows

† Email address for correspondence: vagesh@iitm.ac.in

in the sense that the total shear stress in pCf is constant across the channel. As in other canonical flows, turbulence brings complexity to pCf. Therefore, specially designed experiments and direct numerical simulations (DNS) are required to study pCf when it is in the turbulent regime. El Telbany & Reynolds (1980) conducted experiments to study the velocity distribution in fully turbulent pCf and formulated empirical descriptions for velocities in various sublayers. In a follow-up study (El Telbany & Reynolds 1981), they also developed an empirical explanation for stresses near the walls and in the channel core. Experiments to study the various aspects of pCf have an inherent challenge of capturing all higher-order statistics due to complications arising from a moving boundary (Aydin & Leutheusser 1979). DNS do not have such limitations and a study done by Lee & Kim (1991) explored the flow structures in fully turbulent pCf and compared their results with those of the plane Poiseuille flow. The major difference that they have noticed in pCf is the existence of large-scale high- and low-velocity structures elongated in the streamwise direction, which fill the entire channel in the wall-normal direction. The secondary flow that they reported consists of large counter-rotating vortices or roll cells. Later researchers such as Kristoffersen, Bech & Andersson (1993) and Bech *et al.* (1995) also reported roll cells but the mechanism which gave rise to these vortices was not clear. In the investigation by Hamilton, Kim & Waleffe (1995) the mechanism of formation of roll cells and their role in sustaining the elongated streaks was elaborated. They proposed the concept of a regeneration cycle, which comprises three stages: formation of elongated streaks from the streamwise vorticity associated with roll cells, breakdown of streaks to generate three-dimensional vorticity and regeneration of streamwise vorticity. It appears that this cycle sustains the streaks and counter-rotating vortices which are salient to the fully turbulent regime in pCf.

Only a few decades before, research was successful in discovering the flow features that accompany transition in pCf. The earliest transition studies in pCf were reported by Aydin & Leutheusser (1991), Tillmark & Alfredsson (1992), Daviaud, Hegseth & Bergé (1992) and Malerud, Målo/y & Goldburg (1995). Prigent *et al.* (2003) were one of the first researchers to study detailed flow features in transitional pCf. They discovered that the transition takes place through a stage of oblique laminar–turbulent bands, which are periodic in the streamwise and spanwise directions. These bands exist within the range of $Re \in [325, 415]$. Thus, the flow is fully turbulent above the upper threshold ($Re_t \approx 415$) and laminar below the lower threshold ($Re_g \approx 325$). Their experiments were performed in a large-aspect ratio set-up owing to the large wavelengths of the bands. Performing a DNS in a large domain is computationally challenging. Barkley & Tuckerman (2005) were the first to capture transition bands using DNS. They used a tilted domain in place of a large-aspect-ratio domain and thereby save the computational cost. In another study (Barkley & Tuckerman 2007), they focused on the mean flow aspect of transitional pCf. One main highlight from the aforementioned study is that the mean streamwise velocity in the laminar zones in the transitional regime is not linear, which is why research community refer to these regions in the pattern as quasi-laminar. Another significant outcome from their study is a model which connects the wall-normal profiles of mean flow and the Reynolds stresses. The appearance of laminar–turbulent bands does not always require a fully resolved DNS simulation. Under-resolved simulations can also capture the transition pattern but with a reduction in the transitional Reynolds number range (Manneville 2011; Manneville & Rolland 2011). Apart from the difference in critical Reynolds number, all other aspects of the bands remain the same. As mentioned earlier, alternating laminar–turbulent bands demand the computational domain to be very large. The question of how large a domain is needed is of interest. Philip & Manneville (2011)

suggested an answer to this question by simulating transitional pCf in domains of different diagonal lengths ($L = \sqrt{L_x^2 + L_y^2}$, where L_x and L_y are the domain dimensions in the streamwise and spanwise directions, respectively). They found that the spatiotemporal dynamics associated with pattern formation require a domain with a diagonal length of at least $87.3h$ as domains of size less than that yield an abrupt transition from the turbulent regime to the laminar regime without an intermediate pattern stage. Duguet, Schlatter & Henningson (2010) performed a DNS in a large-aspect-ratio system to capture the competition between bands with different angles, which is otherwise impossible to capture in short domains. They also found that a pattern angle of 40° is more probable to arise during band formation as it requires the least initial energy to carry on. Duguet & Schlatter (2013) studied how oblique laminar–turbulent bands emerge from turbulent spots. According to them, the large-scale flow is responsible for advecting the streaks inside the turbulent spots in an oblique fashion, giving rise to oblique laminar–turbulent bands.

It is difficult to find perfectly smooth surfaces in practical engineering applications. Therefore, there is a need to conduct experiments and simulations of fluid flow under the influence of roughness. One of the earlier works that addressed the effect of roughness was by Nikuradse (1933). Nikuradse used a pipe with an inner wall covered with sand grains of varying roughness and measured the pressure drop and bulk velocity to calculate the friction factor. Roughness increases friction and leads to a higher pressure drop. When it comes to turbulent pCf, only very few studies have considered the effect of roughness. In their pCf experiments, Aydin & Leutheusser (1991) used a staggered array of spherical plastic beads as roughness elements on both the walls. They used a towing tank set-up for the purpose. Compared with their smooth case, the hydrodynamically rough case (surprisingly) showed lower values of streamwise velocity fluctuations. One of the first DNS studies in rough turbulent Couette flows was by Javanappa & Narasimhamurthy (2020, 2021, 2022). They placed square-shaped two-dimensional (2-D) roughness elements on the stationary wall, and the moving wall was smooth. Their study reveals the presence of counter-rotating secondary vortices aligned in the streamwise direction in both the smooth and the rough cases. In the rough case, the streaks are distorted and reduced to fine-scale structures near the roughness elements. Even fewer studies have considered the effect of roughness on the transition to turbulence in pCf. Ishida *et al.* (2017) studied the influence of roughness on transitional pCf. They, however, did not use actual roughness elements, but a roughness model proposed by Busse & Sandham (2012) was used. In the case of one rough wall, a new regime involving transverse turbulent bands was found for all roughness heights greater than 30 % of half-channel height. Another observation is a downwards shift in the transitional range due to roughness. Tsukahara *et al.* (2018) conducted a follow-up study to confirm the existence of transverse turbulent bands. They quadrupled the domain size and studied its influence. Even though the bandwidth changes, the transverse turbulent bands remain robust to domain change. As opposed to oblique turbulent bands, transverse turbulent bands are wider and do not exhibit significant band parallel flow. Another difference is the presence of very intense streaks at the laminar–turbulent interfaces of transverse turbulent bands.

Most experimental and numerical studies dealt with the transition to turbulence in pCf considered smooth walls. Only a few works in the literature study the effect of roughness on transition in pCf, and none of them has used real roughness elements. The present study is, thereby, novel as it intends to study transition in pCf in the presence of real roughness elements. Particular attention is given to studying the various aspects such as spatiotemporal intermittency, large-scale flow, mean secondary flow and Reynolds

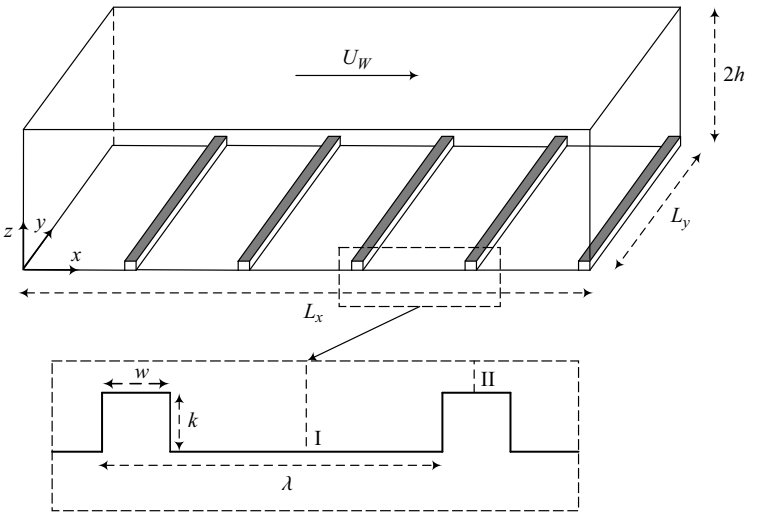

Figure 1. Schematic of rough Couette flow with roughness elements on the stationary wall. Within a pitch, I and II indicate the midcavity and midrib locations, respectively.

stresses, in rough pCf. We also investigate the effect of pitch separation of 2-D roughness elements on the transitional range.

2. Methodology

A schematic of rough pCf is shown in figure 1. Two parallel plates are separated by a wall-normal (z) distance of $2h$. Here L_x and L_y are the dimensions of the computational domain in the streamwise (x) and spanwise (y) directions, respectively. The top plate moves at a constant velocity U_w in the x direction, and the bottom plate is stationary. The stationary wall is mounted with 2-D roughness elements. The important parameters in rough Couette flows are the roughness height (k), the width (w) and the streamwise pitch separation (λ). We use roughness elements of height $k = 0.2h$ with a square cross-section ($k = w$) and vary the pitch separation to study its influence on transition to turbulence. Perry, Schofield & Joubert (1969) classified surface roughness as d-type and k-type roughness. In the d-type roughness, the elements are closely spaced, forming stable recirculations in the narrow cavities. The outer flow is relatively undisturbed as vortex shedding above the roughness crest is negligible. In the k-type roughness, the cavities are wide; therefore, the ribs are subjected to the outer flow. Eddies of a length scale proportional to k are shed above the roughness crest. According to Jiménez (2004), the roughness behaviour transitions from d-type to k-type when the cavities become wider than three to four times the roughness height k. The relative importance of frictional drag compared with pressure drag varies with the type of roughness. In the d-type roughness, frictional drag dominates, whereas in the k-type roughness, pressure drag is more significant (Leonardi, Orlandi & Antonia 2007). In the present study, we have the d-type ($\lambda = 2k$) and the k-type ($\lambda = 10k$) rough cases. Transition to turbulence in the smooth pCf is also simulated for comparison with the rough pCf.

The fluid that occupies the gap between the parallel plates is Newtonian, and the flow is considered incompressible. The three-dimensional incompressible Navier Stokes equations that govern the fluid flow are solved using the in-house finite-volume code,

MGLET (Manhart 2004):

$$\frac{\partial u_i}{\partial x_i} = 0, \tag{2.1}$$

$$\frac{\partial u_i}{\partial t} + u_j \frac{\partial u_i}{\partial x_j} = -\frac{\partial p}{\partial x_i} + \frac{1}{Re} \frac{\partial^2 u_i}{\partial x_j^2}, \tag{2.2}$$

where u is the velocity, the subscripts i and j are indices and p is the pressure. The Reynolds number ($Re = U_w h/2\nu$) is defined based on the half-channel height (h) and half the velocity difference between the plates ($U_w/2$). The code uses a staggered Cartesian grid arrangement, where the pressure is stored at the cell centres, and velocities are stored at the cell faces. It employs a central difference scheme for spatial discretisation. Adams–Bashforth scheme (second-order accurate) is used to perform time integration. A multi-grid method is used to accelerate the Poisson equation solution to get the pressure. Streamwise and spanwise directions of the domain have periodic boundary conditions, and a no-slip boundary condition is imposed on the plates and the rib surfaces.

A computational domain of size $L_x \times L_y \times L_z = 136h \times 68h \times 2h$ is used in the present study. It is large enough to accommodate a single wavelength of the laminar–turbulent bands and is of the same size as Ishida *et al.* (2017) (see table 1). The number of cells in the x, y and z directions (N_x, N_y and N_z) is 4080, 288 and 108, respectively, and is finer than that used in Ishida *et al.* (2017) and Tsukahara *et al.* (2018). The grid in the x and y directions is uniform, whereas the grid in the z direction is non-uniform, with a minimum at the plates and the rib surfaces and a maximum at the channel centre. The meshing is done in such a way that all the vertical faces of the ribs coincide with the cell faces. To get an accurate assessment of the flow near a rib, we have 6 cells along a rib in the x direction and 20 cells within a rib in the z direction. The grid resolutions for the rough cases are given in table 2. We have used the same domain for the smooth case, but the mesh size is different. The grid resolutions in the x and z directions are reduced as the ribs are not present in the smooth pCf (see table 2). The Grötzbach criterion states that the grid size $\Delta = (\Delta x \Delta y \Delta z)^{1/3}$ should be less than $\pi\eta$, where η is the Kolmogorov length scale (Grötzbach 1983). The Kolmogorov length scale is defined in theory as $\eta = (\nu^3/\epsilon)^{1/4}$, where ν is the kinematic viscosity of the fluid, and ϵ is the dissipation rate of turbulent kinetic energy, which is calculated using the expression $\epsilon = \nu\overline{(\partial u_i'/\partial x_j)(\partial u_i'/\partial x_j)}$. The grids used in all the cases in the present study satisfy the Grötzbach criterion (see figure 2).

An adiabatic protocol (Ishida *et al.* 2017; Gokul & Narasimhamurthy 2022) is a computational procedure, where the Reynolds number is gradually reduced in steps. The term adiabatic protocol comes from the adiabatic process in quantum mechanics, where it is used as synonym for a gradual process. It should not be mistaken for the adiabatic process in thermodynamics, as it has a different meaning. This computational technique is used in the present study to achieve the reverse transition. Starting from a turbulent state at $Re = 500$, the Reynolds number is reduced in steps of 25 until the flow becomes laminar. Statistical stationarity has been achieved at every intermediate Reynolds number. The time step taken in the simulations ($\Delta t = 0.01$) is much smaller than the Kolmogorov time scale (Kolmogorov 1941) and satisfies the Courant–Friedrichs–Lewy (CFL) stability criterion. After achieving stationarity at a particular Reynolds number, the simulation is run further to collect samples for getting the averaged quantities. The mean values are obtained by averaging over 2500 samples separated by $0.2h/U_w$. The wall-normal variation of mean quantities for the rough pCf cases will be presented at the midcavity (I) and midrib (II) locations, obtained by averaging across time (T), y direction and the pitches (N) in the x

https://doi.org/10.1017/jfm.2024.844 Published online by Cambridge University Press

Reference	Case	k	λ	$L_x \times L_y \times L_z$	$N_x \times N_y \times N_z$
Barkley & Tuckerman (2005)	Smooth	—	—	$10h \times 120h \times 2h$ (tilted domain)	$61 \times 1024 \times 31$
Barkley & Tuckerman (2007)	Smooth	—	—	$10h \times 40h \times 2h$ (tilted domain)	$81 \times 512 \times 41$
Duguet *et al.* (2010)	Smooth	—	—	$800h \times 386h \times 2h$	$2048 \times 1024 \times 33$
Philip & Manneville (2011)	Smooth	—	—	$5\pi h \times 2\pi h \times 2h$	$64 \times 32 \times 33$
				$24h \times 9h \times 2h$	$94 \times 32 \times 33$
				$32h \times 15h \times 2h$	$128 \times 64 \times 33$
				$60h \times 26h \times 2h$	$192 \times 96 \times 33$
				$70h \times 30h \times 2h$	$282 \times 128 \times 33$
				$80h \times 35h \times 2h$	$384 \times 192 \times 33$
				$90h \times 40h \times 2h$	$384 \times 192 \times 33$
				$100h \times 45h \times 2h$	$384 \times 192 \times 33$
				$128h \times 64h \times 2h$	$512 \times 256 \times 33$
Manneville (2011)	Smooth	—	—	$432h \times 256h \times 2h$	$432 \times 768 \times 15$
Duguet & Schlatter (2013)	Smooth	—	—	$500h \times 500h \times 2h$	$1536 \times 2048 \times 33$
Ishida *et al.* (2017)	Rough	$0.05h$–$0.5h$	—	$136h \times 68h \times 2h$	$512 \times 256 \times 96$
Tsukahara *et al.* (2018)	Rough	$0.15h$–$0.5h$	—	$272h \times 136h \times 2h$	$1024 \times 512 \times 96$
				$1088h \times 68h \times 2h$	$4096 \times 256 \times 96$
Present study	Smooth	—	—	$136h \times 68h \times 2h$	$576 \times 288 \times 96$
Present study	Rough (d-type)	$0.2h$	$2k$	$136h \times 68h \times 2h$	$4080 \times 288 \times 108$
Present study	Rough (k-type)	$0.2h$	$10k$	$136h \times 68h \times 2h$	$4080 \times 288 \times 108$

Table 1. Details of the major DNS studies in transitional pCf. Here k and λ are the roughness height and pitch, respectively, L_x, L_y and L_z refer to the domain dimensions in x, y and z, respectively and N_x, N_y and N_z is the corresponding number of cells or grid points or spectral modes.

Case	$L_x \times L_y \times L_z$	$N_x \times N_y \times N_z$	Δx^+	Δy^+	Δz^+_{min}	Δz^+_{max}
Smooth	$136h \times 68h \times 2h$	$576 \times 288 \times 96$	5.33–8.72	5.33–8.72	0.23–0.37	0.83–1.36
d-type	$136h \times 68h \times 2h$	$4080 \times 288 \times 108$	0.81–1.25	5.75–8.88	0.24–0.38	0.87–1.34
k-type	$136h \times 68h \times 2h$	$4080 \times 288 \times 108$	0.75–1.42	5.30–10.07	0.23–0.43	0.80–1.52

Table 2. Details of the simulations carried out in the present study. The grid resolutions (Δx^+, Δy^+ and Δz^+) are based on the global friction Reynolds number Re_τ of each case.

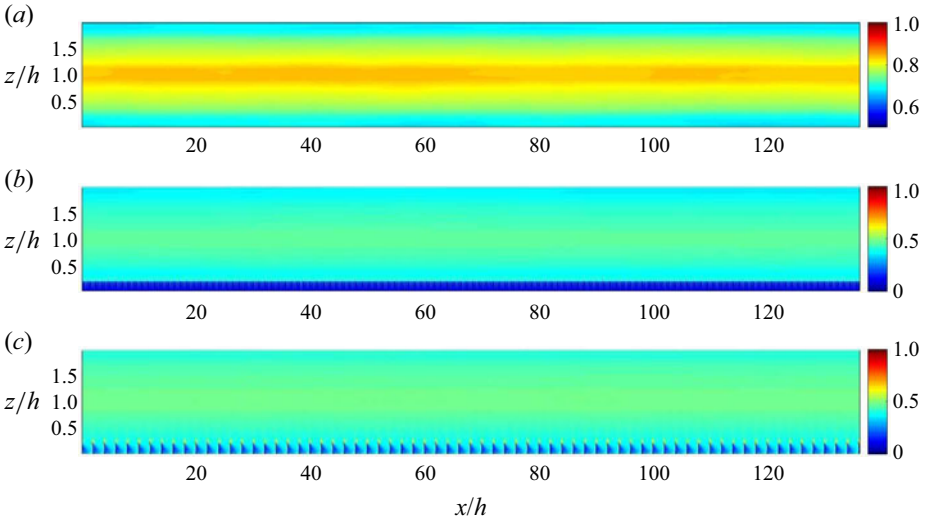

Figure 2. Contours of $\Delta/\pi\eta$ at $Re = 500$ shown in an x–z plane at $y = 34h$ for (a) smooth pCf, (b) d-type roughness and (c) k-type roughness.

direction:

$$\bar{f} = \frac{1}{N}\frac{1}{L_y}\frac{1}{T}\sum_{1}^{N}\int_0^{L_y}\int_0^{T} f \,\mathrm{d}t\,\mathrm{d}y. \tag{2.3}$$

The averaging across the pitches in the x direction is due to the periodic nature of the mean flow (Ashrafian, Andersson & Manhart 2004; Nagano, Hattori & Houra 2004; Javanappa & Narasimhamurthy 2021). However, the mean quantities in the smooth pCf are averaged across time (T), y and x directions:

$$\bar{f} = \frac{1}{L_x}\frac{1}{L_y}\frac{1}{T}\int_0^{L_x}\int_0^{L_y}\int_0^{T} f \,\mathrm{d}t\,\mathrm{d}y\,\mathrm{d}x. \tag{2.4}$$

Before embarking on the current problem, a smooth pCf case at $Re = 1300$ is simulated to validate the code. The computational domain used for the validation case is of size $L_x \times L_y \times L_z = 50.24h \times 16.8h \times 2h$. The corresponding grid used is $N_x \times N_y \times N_z = 640 \times 320 \times 192$. The grid resolutions are uniform in x and y directions ($\Delta x^+ = 6.64$ and $\Delta y^+ = 4.44$), whereas the grid resolution in z direction is non-uniform and varies from $\Delta z^+ = 0.2$ at the walls to $\Delta z^+ = 2.3$ at the channel centre. The results are plotted along with those from Bech *et al.* (1995), Holstad, Andersson & Pettersen (2010) and Hu, Morfey & Sandham (2003) (see figure 3). The validation results are in good agreement.

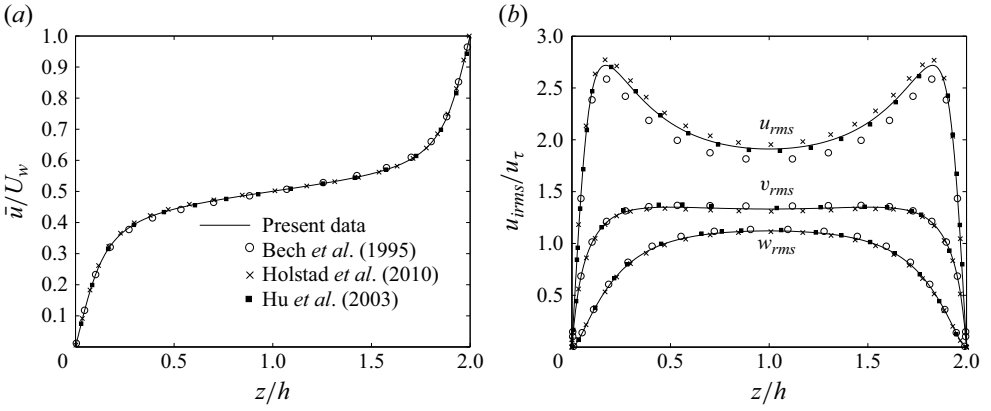

Figure 3. Variation of (*a*) mean streamwise velocity normalised by U_w and (*b*) root-mean-square velocities normalised by friction velocity u_τ at $Re = 1300$.

3. Results and discussion

We first simulate the base flow at $Re = 500$ before starting the adiabatic procedure. The flow is allowed to come to a stationary state before the samples are collected to calculate the averaged quantities. The turbulent flow statistics at $Re = 500$ for the rough pCf cases are presented in Appendix A for the reader's reference. The Reynolds number is gradually reduced in steps of 25 from $Re = 500$ until the flow reaches a laminar state. The results presented at every intermediate Reynolds number are obtained after achieving a statistical stationary state at the intermediate stage. The contours of streamwise velocity u in the midgap ($z = h$) for the d-type roughness at various Reynolds numbers are shown in figure 4. The flow is turbulent for $Re \geq 475$. The turbulent flow is characterised by spanwise alternating high- and low-velocity streaks stretching out in the streamwise direction. When the Reynolds number is reduced to 450, a few laminar spots appear in the turbulent surroundings. At this point, the laminar–turbulent coexistence has not developed into the laminar–turbulent bands. Kashyap, Duguet & Dauchot (2022) have provided evidence that the pattern stage emerges from the spatial modulation of featureless turbulence caused by linear instabilities. Without disregarding the effect of such linear interactions, Gomé, Tuckerman & Barkley (2023*b*) established a more complex mechanism involving the laminar spots. They found that a reduction in Re yields laminar spots that are more probable and long-lasting, which eventually self-organise and form regular laminar–turbulent bands. On reducing the Reynolds number to $Re = 425$, oblique laminar–turbulent bands become visible. There is an initial transient during which pattern fronts of different angles compete, and stable bands eventually emerge in the flow field (Prigent *et al.* 2003). These stable patterns are observed for all Reynolds numbers in the range $Re \in [350, 425]$. In the present study, all observations in the transitional range are made after the emergence of stable laminar–turbulent bands. In the presence of transient turbulence, a shorter observation time can adversely affect the results (Bottin & Chaté 1998; Hof *et al.* 2006; Avila *et al.* 2011; Avila, Barkley & Hof 2023). Therefore, statistical stationarity has been achieved at all Re considered in this study. The width of the turbulent bands shrink with a reduction in Reynolds number, which indicates flow shifting gradually towards the laminar regime. On reducing the Reynolds number to $Re = 325$, the turbulent bands shrink further and finally disappear from the flow field, resulting in a laminar flow. In the k-type roughness, the flow remains turbulent for Reynolds numbers up to $Re = 375$

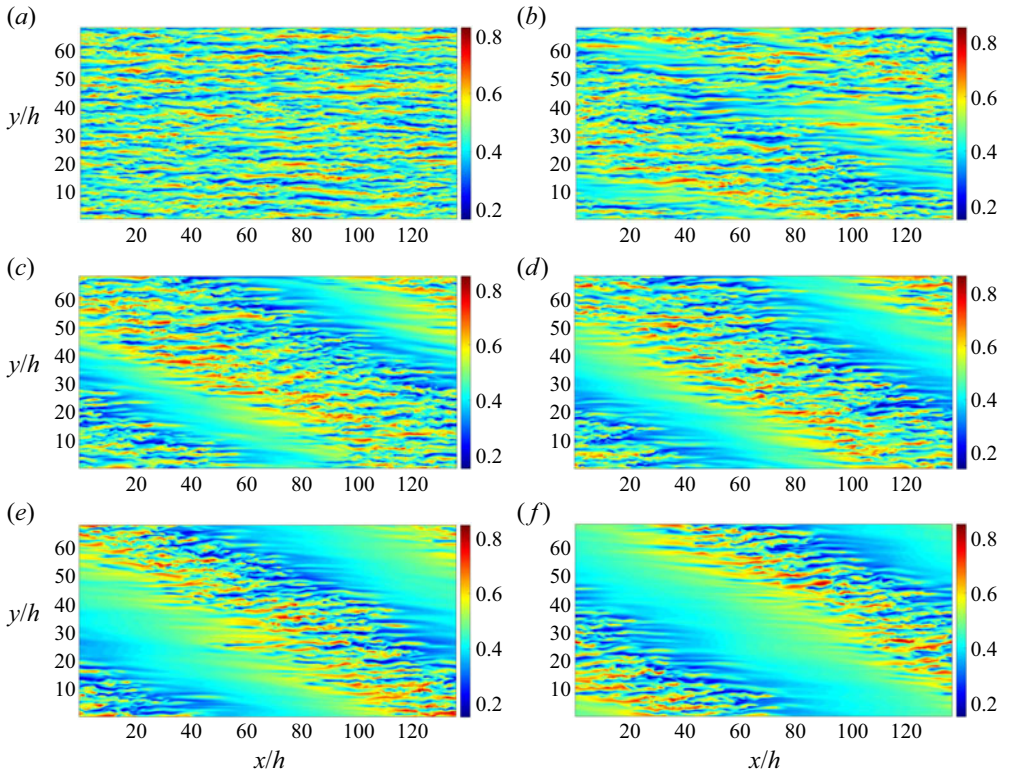

Figure 4. Streamwise velocity (u) at the midgap location ($z = h$) for d-type roughness at (a) $Re = 500$, (b) $Re = 450$, (c) $Re = 425$, (d) $Re = 400$, (e) $Re = 375$ and (f) $Re = 350$.

(see figure 5). A further reduction to $Re = 350$ yields a few laminar spots in the turbulent environment. The laminar–turbulent coexistence takes the form of laminar–turbulent bands at $Re = 325$, and they are sustained in the flow up to $Re = 300$. Therefore, the bands are stable for all Reynolds numbers in the range $Re \in [300, 325]$. Similar to the d-type roughness, there is a reduction in the width of turbulent bands when the Reynolds number is decreased. The flow finally laminarises at $Re = 275$.

The smooth pCf is known to have stable bands for Reynolds numbers in the range $Re \in [325, 400]$ (Ishida *et al.* 2017; Gokul & Narasimhamurthy 2022). Compared with the smooth pCf, the transitional range for the k-type roughness has shifted downwards ($Re \in [300, 325]$), and the corresponding range for the d-type roughness has moved upwards ($Re \in [350, 425]$). We need to understand why the roughness causes a shift in the transitional range. The streamwise vorticity plays a crucial role in the formation and sustenance of the elongated streaks that constitute the turbulent bands. The regeneration cycle proposed by Hamilton *et al.* (1995) thoroughly explains this relationship in the smooth pCf. The streamwise vorticity decays as it produces the elongated streaks through a redistribution of momentum (lift-up effect). The streaks thus formed develop a waviness and eventually break down, releasing vorticity in all three directions, which also regenerates the streamwise vorticity. The reenergised streamwise vorticity will again form elongated streaks, thus completing a cycle. However, the roughness elements interfere with the near-wall flow dynamics and modify the regeneration cycle, most likely weakening it (Jiménez 2004). Therefore, the roughness should offer an additional mechanism for

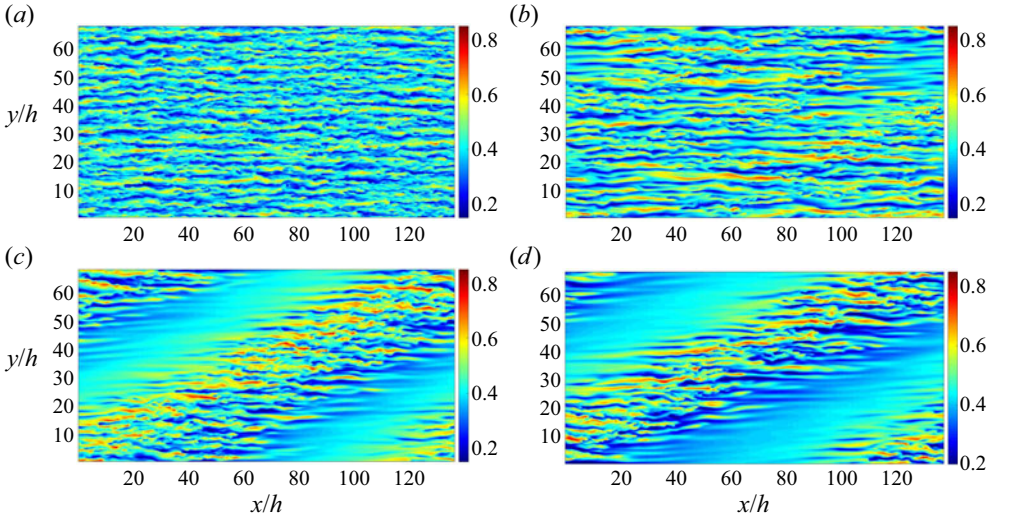

Figure 5. Streamwise velocity (u) at the midgap location ($z = h$) for k-type roughness at (a) $Re = 500$, (b) $Re = 350$, (c) $Re = 325$ and (d) $Re = 300$.

regenerating the streamwise vorticity. Figure 6 shows the streamwise vorticity in an x–z plane at the midspan location for the current rough pCf cases within the transitional regime. In the k-type roughness, vortices are generated within the cavities and are eventually shed from the roughness elements into the outer flow. On the other hand, the d-type roughness does not exhibit the same type of vortex shedding as the k-type roughness. The stable vortices in the cavities of the d-type roughness (to be discussed in conjunction with figure 13(a), presented later) act as a deterrent to vortex shedding (Perry *et al.* 1969; Coleman *et al.* 2007). However, not all turbulent events near the cavities can be ruled out, as there can be occasional ejections (Townsend 1976). Jiménez (2004) and Leonardi *et al.* (2004) also confirmed the occurrence of ejections from the cavities of the d-type roughness. However, the intensity of these events is lower than that observed in the k-type roughness (Leonardi *et al.* 2007). Even if we account for these events in the d-type roughness, given their sporadic and weak nature, their contribution to vorticity regeneration is likely insignificant. In contrast, the ribs in the k-type roughness act as vortex generators and function as an alternate source for streamwise vorticity regeneration. Therefore, the k-type roughness can sustain stable laminar–turbulent bands at lower Reynolds numbers than the d-type roughness and the smooth pCf. However, the d-type roughness causing an upwards shift in the transitional range compared with the smooth pCf can come across as a surprise. Choi & Fujisawa (1993) studied the development of a zero-pressure-gradient turbulent boundary layer over a flat plate with a square cavity similar to that in a d-type roughness. They found that the stable recirculation zone in the cavity alters the near-wall flow dynamics, which reduces the incidence of turbulent events compared with a smooth boundary layer. Therefore, exploring the vortical structures within the near-wall region can provide further insights. Figures 7(a) and 7(b) shows the isosurfaces of $-\lambda_2$ for the rough pCf cases within the transitional regime, providing a visualisation of vortical structures, as defined by Jeong & Hussain (1995) [vortical structures corresponding to a smooth pCf are also shown in figure 7(c) for comparison]. Here λ_2 is defined as the second largest eigenvalue of the tensor $\boldsymbol{S}^2 + \boldsymbol{\Omega}^2$, where $\boldsymbol{S}$ and $\boldsymbol{\Omega}$ are the symmetric and antisymmetric parts of the velocity gradient tensor, respectively.

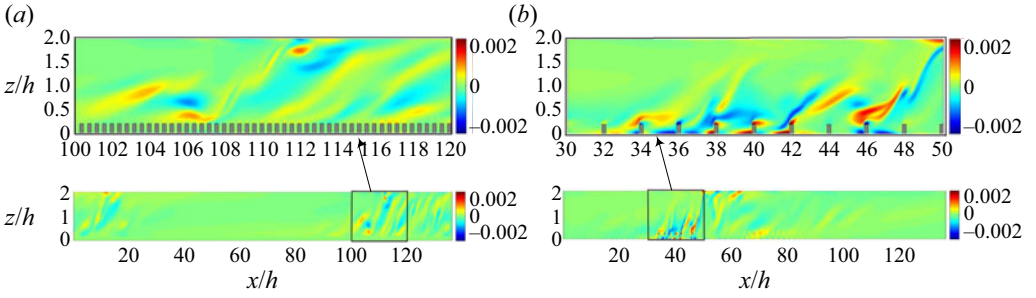

Figure 6. Instantaneous streamwise vorticity (ω_x) in an x–z plane at $y = 34h$ for (*a*) d-type roughness ($Re = 350$) and (*b*) k-type roughness ($Re = 300$). Vorticity values are normalised by ${U_w}^2/\nu$.

A closer examination of the near-wall structures shows a clear distinction between the rough pCf cases. Also note the striking similarity between the k-type roughness and the smooth pCf. In the d-type roughness, the near-wall region is dominated by vortical structures oriented in the spanwise direction. Compared with the k-type roughness and the smooth pCf, the streamwise-oriented vortical structures in the d-type roughness are away from the stationary wall, resulting in a relatively stable region close to the wall. Luchini, Manzo & Pozzi (1991) have attributed the drag-reducing nature of riblets to a similar shift of the turbulent structures away from the wall. This could lead to reduced disturbances and increased stability near the stationary wall, which can negatively affect the formation and sustenance of streaks. Consequently, the d-type roughness cannot sustain the elongated streaks that constitute the turbulent bands as effectively as the smooth pCf. As a result, the flow in the d-type roughness laminarises at a higher Reynolds number than the smooth pCf.

The pattern of laminar–turbulent bands is periodic in the streamwise and spanwise directions. It has large wavelengths in both these directions. The experiments by Prigent *et al.* (2003) suggest that these wavelengths are sensitive to changes in Reynolds number. However, the pattern wavelengths obtained for the rough pCf cases in the present study remain unchanged with the Reynolds number. We have also observed this phenomenon in our previous study on the smooth pCf (Gokul & Narasimhamurthy 2022). The wavelengths λ_x and λ_y are always equal to the domain dimensions L_x and L_y, respectively, due to the influence of the periodic boundary condition. This phenomenon is inevitable in numerical simulations not performed in large-aspect-ratio systems. The transition study by Ishida *et al.* (2017), who used a similar domain as ours, also observed the same. Tsukahara, Kawaguchi & Kawamura (2009) used a much larger domain and found their wavelengths remain unchanged with Reynolds number due to the influence of periodic boundary conditions. As the pattern wavelengths for rough pCf cases in the present study are equal to the corresponding domain dimensions, the pattern will consistently align with one of the domain diagonals. Therefore, the angle made by the pattern (with x direction) in the d-type and the k-type roughness is approximately equal to 27°. The pattern angle in the smooth pCf is the same as that of the rough pCf cases.

Large-scale flow is key in understanding the obliqueness of the laminar–turbulent bands. It is responsible for advecting the streaks in the turbulent spots in an oblique fashion, which later develop to form oblique bands (Duguet & Schlatter 2013). There is a pronounced scale separation between the turbulent fluctuations that constitute the streaks and the large-scale flow associated with the laminar–turbulent bands (Gomé, Tuckerman & Barkley 2023*a*). A low-pass filter can extract the large scales linked to the pattern (Ishida,

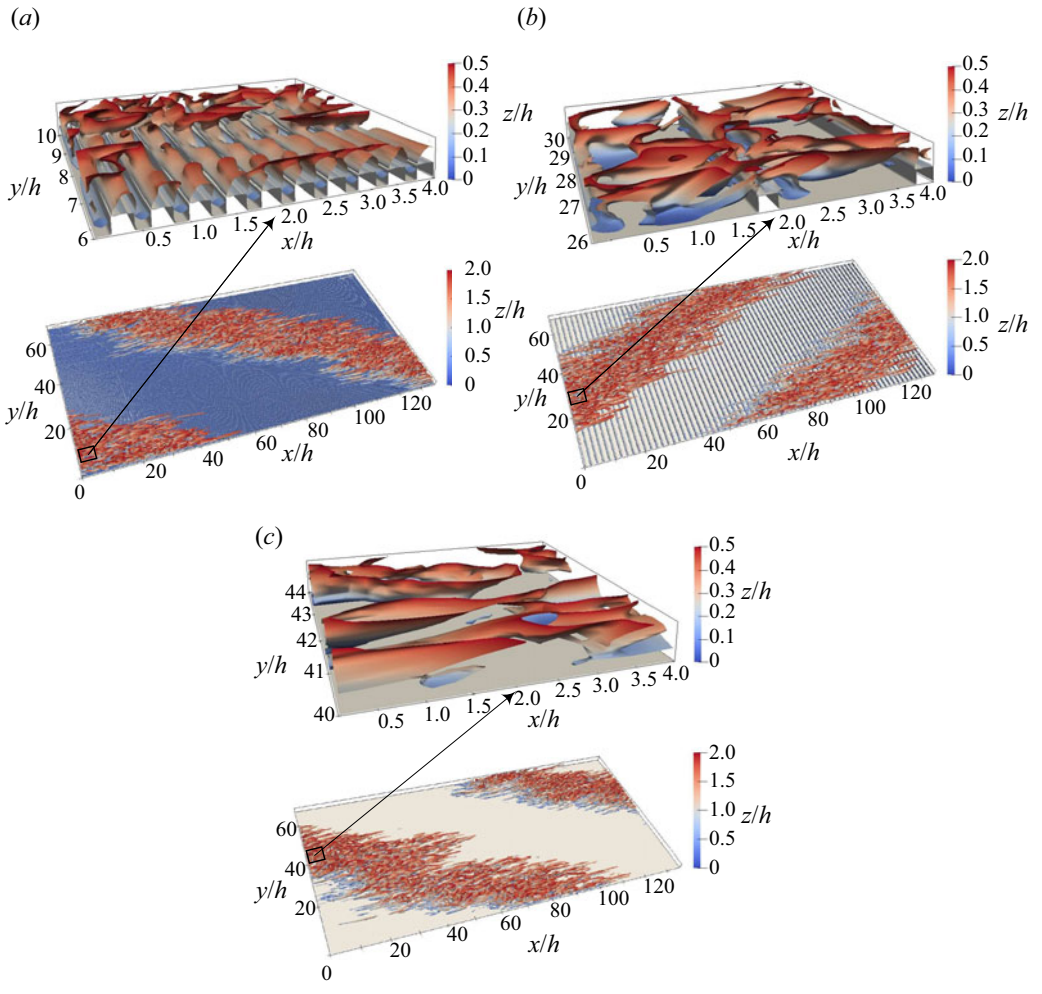

Figure 7. Isosurface of $\lambda_2 = -1 \times 10^{-8}$ coloured with the variation in z/h for (*a*) d-type roughness ($Re = 350$), (*b*) k-type roughness ($Re = 300$) and (*c*) smooth pCf ($Re = 325$). Here λ_2 values are normalised using ${U_w}^4/\nu^2$. Top panels show enlarged views of a small region (shown by arrows).

Duguet & Tsukahara 2017; Tsukahara *et al.* 2018). Figure 8 shows wall-normal averaged large-scale flow vectors (obtained through low-pass filtering) along with the contours of streamwise velocity fluctuations ($u' = u - \bar{u}$, where $\bar{u}$ is the mean streamwise velocity obtained by time averaging) in the background for the d-type and the k-type roughness. The flow is parallel to the oblique bands near the laminar–turbulent boundaries, implying a significant spanwise velocity component in the large-scale flow. The probability density function of the angle β made by the large-scale flow vectors (with x direction) is shown in figure 9. The peak probability for the d-type and the k-type roughness is at 24°, which matches well with the pattern angle.

The transition to turbulence in pCf is spatiotemporal (Philip & Manneville 2011). Spatiotemporal diagrams (figures 10 and 11) help understand the dynamics of laminar–turbulent bands. This diagram represents data recorded across both space and time. The time series data of streamwise velocity u are collected at 288 equidistant points along a spanwise line located at the centre of the domain ($x = 68h$, $z = h$) for a

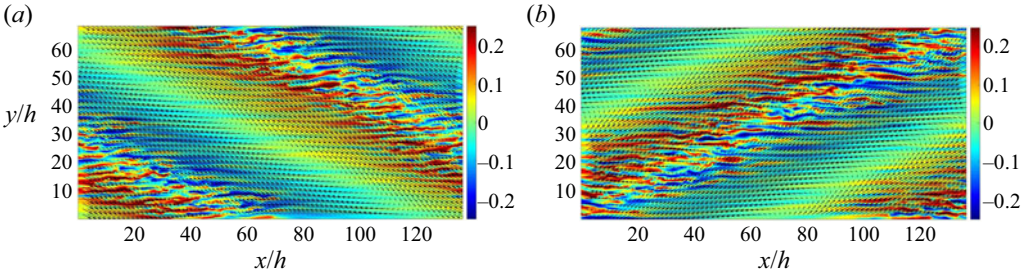

Figure 8. Streamwise velocity fluctuations (u') at the midgap location ($z = h$) and the corresponding wall-normal-averaged large-scale flow ($\bar{U}, \bar{V}$) for (*a*) d-type roughness ($Re = 350$) and (*b*) k-type roughness ($Re = 300$).

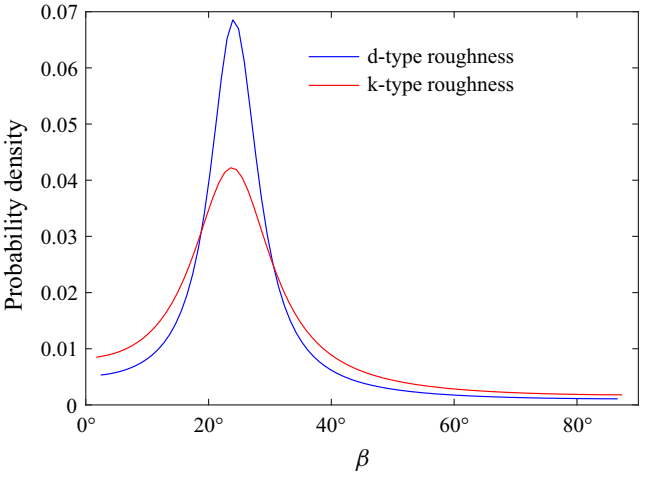

Figure 9. Probability distribution function of angle β made by the large-scale flow vectors. The probability density gives the likelihood associated with various orientations of the large-scale flow vectors.

total time of $1000h/U_w$. The spatiotemporal data are recorded after a stable pattern has emerged to avoid the initial transients in the flow. The laminar–turbulent coexistence in the spatiotemporal plane also yields oblique bands like a streamwise–spanwise (x–y) plane. The effect of the Reynolds number on the spatiotemporal dynamics is such that there is a reduction in the area occupied by the turbulent regions as the Reynolds number is reduced. This reduction in the turbulent area indicates flow being turbulent at fewer points and for lesser duration of time. The frequency of the pattern in the spatiotemporal plane is found using a fast Fourier transform (FFT). Figure 12 shows the spectral analysis for the rough pCf cases. The most energetic frequencies associated with the pattern for the d-type and the k-type roughness are 3.81×10^{-3} and 3.05×10^{-3}, respectively. The corresponding time period can be found by taking the reciprocal of peak frequency. Therefore, the time period of the pattern in the d-type and the k-type roughness are $262.14h/U_w$ and $327.67h/U_w$, respectively. The peak frequency and time period do not change with the Reynolds number within the transitional regime. Having the wavelength ($\lambda_x \approx 136h$) and frequency already established, one can ascertain the speed of the wave in the x direction. The calculated wave speeds for the d-type and the k-type roughness are approximately $0.52U_w$ and $0.41U_w$, respectively. It is interesting to note that these speeds compares well with the respective

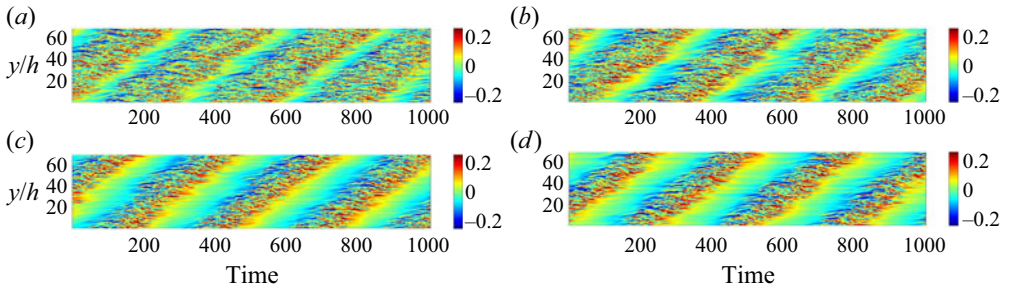

Figure 10. Streamwise velocity fluctuations (u') in a spatiotemporal plane for d-type roughness at (a) $Re = 425$, (b) $Re = 400$, (c) $Re = 375$ and (d) $Re = 350$.

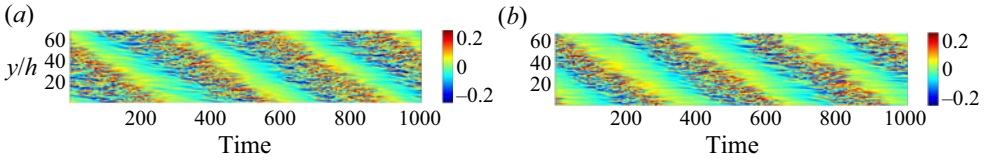

Figure 11. Streamwise velocity fluctuations (u') in a spatiotemporal plane for k-type roughness at (a) $Re = 325$ and (b) $Re = 300$.

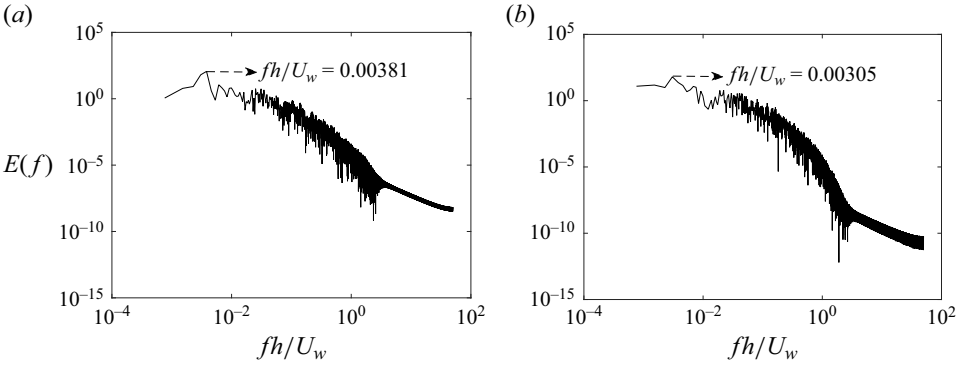

Figure 12. Frequency-based representation of streamwise velocity u for (a) d-type roughness ($Re = 350$) and (b) k-type roughness ($Re = 300$).

mean streamwise velocities at the apparent midgap locations of the rough pCf cases (the locations of apparent midgaps and their corresponding mean streamwise velocities are shown in Appendix A.2). Similarly, the mean band speed in the smooth pCf closely matches the mean streamwise velocity in the midgap (Gokul & Narasimhamurthy 2022).

In the subsequent analysis, our focus is on exploring the mean flow characteristics of the rough pCf cases. In the transitional regime, the mean quantities have contributions from the turbulent and quasi-laminar regions of the flow field. This aspect is crucial when interpreting the mean quantities in the transitional regime. In the rough pCf cases, data are averaged across pitches, in addition to averaging over time and the y-direction. Figure 13 illustrates the mean streamlines for the near-wall region superimposed on the contours of mean streamwise velocity for the transitional regime. The narrow cavity in the d-type roughness forms a single recirculation zone. This vortex is stable (Perry *et al.* 1969) and thus shields the outer flow from interacting with the wall or cavity floor in the d-type case.

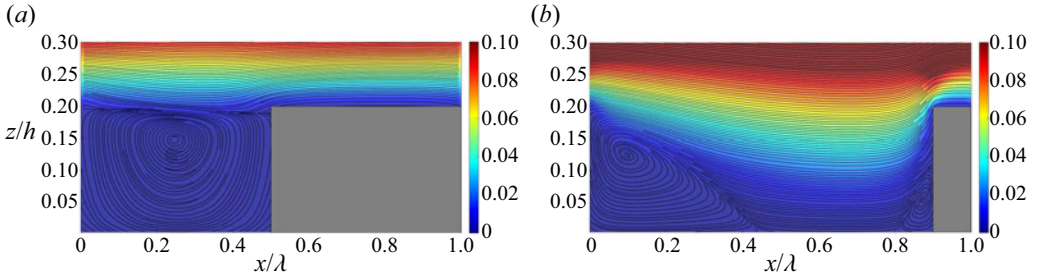

Figure 13. Mean streamlines with contours of mean streamwise velocity in the background for (*a*) d-type roughness ($Re = 350$) and (*b*) k-type roughness ($Re = 300$). Here, x is normalised by the pitch λ instead of h.

The vortex is relatively weak (Leonardi *et al.* 2007), resembling a low-velocity, 2-D, lid-driven cavity flow (Cui, Patel & Lin 2003). Therefore, the mean streamwise velocity within the cavity is significantly lower compared with that of the outer flow. The corresponding friction coefficient ($C_f = \nu(\partial\bar{u}/\partial z)/U_w^2$) on the cavity floor is negligible, indicating that the wall shear stress is practically zero (see figure 14*a*). This resembles a free-slip boundary, which can likely contribute to the stability of the recirculation zone within the cavity in the d-type roughness. In contrast, C_f is non-zero on the rib crest. Therefore, the near-wall flow in the d-type case experiences alternate free-slip-like (on the cavity floor) and no-slip (on the rib crest) conditions along the x direction. MacDonald *et al.* (2018) drew an analogy between the mean flow over the d-type roughness and superhydrophobic surfaces, where liquid flows over gas-filled cavities between roughness elements, presenting alternating zero-shear/zero-velocity conditions. This analogy implies that, similar to superhydrophobic surfaces where the liquid skims past the cavities, there is limited interaction between the outer flow and the cavities in the d-type roughness. In the k-type roughness, the flow separates near the trailing edge of the rib and later reattaches to the cavity floor, forming a large vortex near the trailing face and a smaller vortex close to the leading face of the next rib. These vortices are unstable and lead to significant vortex shedding above the rib crests (Perry *et al.* 1969). The mean streamwise velocity within the cavity is higher than that of the d-type roughness as the ribs are subjected to the outer flow. The C_f along the cavity floor is initially negative due to the large recirculation bubble (see figure 14*b*). It then shifts to positive upon reattachment and returns to negative due to the small recirculation bubble near the next rib. Further, on the rib crest, the C_f is at its maximum near the leading edge and gradually reduces along its length. The mean velocity profiles for the rough pCf cases in the transitional regime are shown in figure 15. The mean velocity values are plotted at the midcavity (I) and midrib (II) locations and compared with those from the smooth pCf. It is well known that the variation of mean streamwise velocity $\bar{u}$ has the typical S-shape in the smooth pCf. Compared with the smooth pCf, $\bar{u}$ in rough pCf cases is reduced due to the blockage offered by the roughness. This reduction in the magnitude of $\bar{u}$ is more pronounced near the rib-roughened stationary wall and reduces as we approach the smooth moving wall. The $\bar{u}$ variations at I and II locations follow distinct paths close to the stationary wall but collapse beyond $z = 0.5h$ in the d-type roughness. However, in the k-type roughness, the $\bar{u}$ variations at I and II follow different paths until the channel centre ($z = h$) before collapsing.

Table 3 presents the values of friction velocity u_τ and the corresponding friction Reynolds number Re_τ for the d-type and the k-type roughness (the corresponding values for the smooth pCf are also given for comparison). Note that the friction velocity for the rib-roughened wall is due to both the viscous drag and the pressure drag. The method used

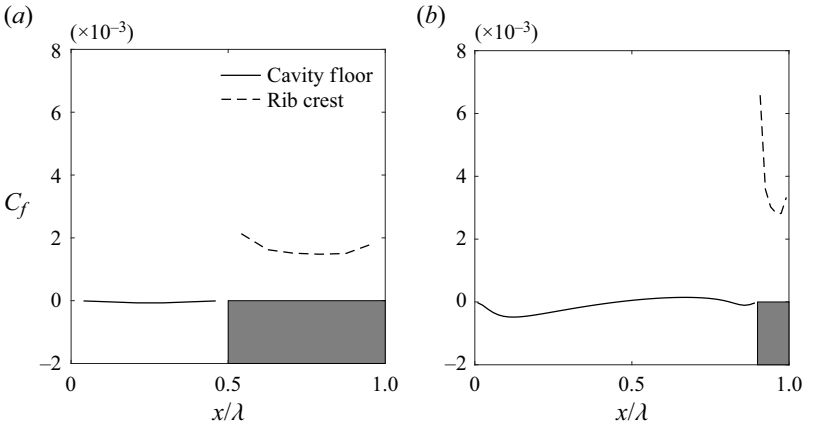

Figure 14. Variation of skin friction coefficient on the cavity floor and rib crest for (*a*) d-type roughness ($Re = 350$) and (*b*) k-type roughness ($Re = 300$). Here, x is normalised by the pitch λ instead of h.

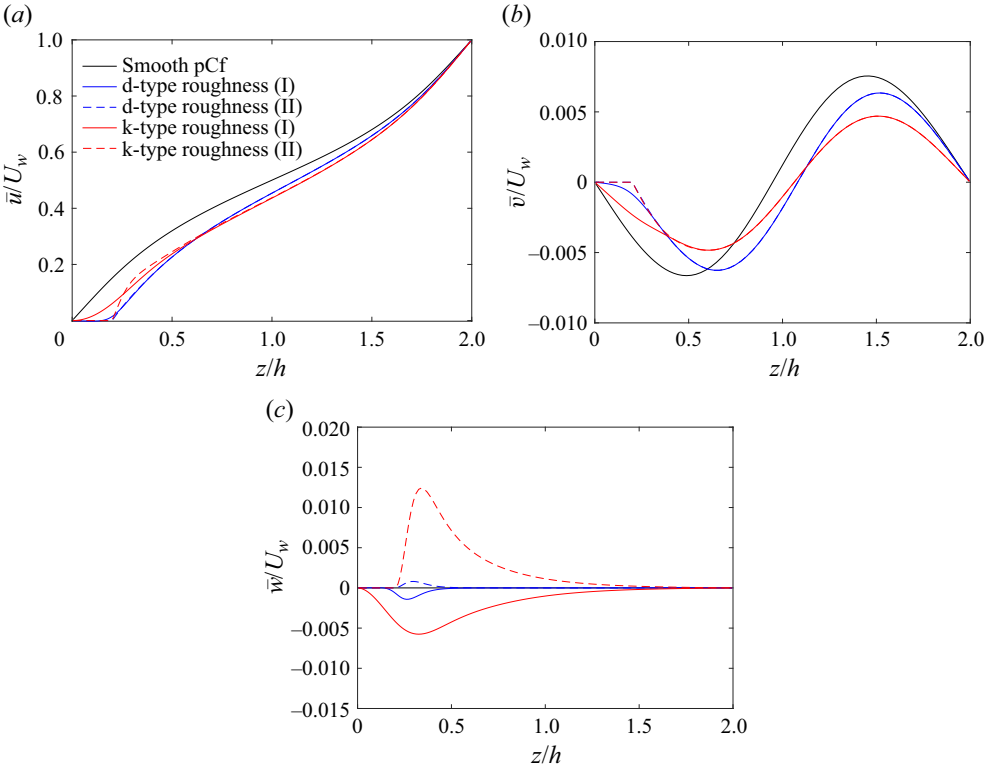

Figure 15. Variation of (*a*) mean streamwise velocity $\bar{u}$, (*b*) mean spanwise velocity $\bar{v}$ and (*c*) mean wall-normal velocity $\bar{w}$ along the wall-normal direction for d-type roughness and k-type roughness at the midcavity (I) and midrib (II) locations at a Reynolds number close to their lower threshold (Re_g). Here Re_g is the Reynolds number in the transitional regime below which the flow turns laminar. Corresponding velocity profiles in smooth pCf are also plotted for comparison.

Case	Smooth pCf	d-type roughness	k-type roughness
Re	500–325	500–350	500–300
$\overline{V_{dS}}$	0.00136–0.00121	9.49×10^{-4}–8.18×10^{-4}	6.55×10^{-5}–2.79×10^{-4}
$\overline{V_{dM}}$	0.00136–0.00121	0.00143–0.00123	0.00185–0.00143
$\overline{P_{dS}}$	—	4.49×10^{-4}–3.68×10^{-4}	0.00172–0.00109
$u_{\tau S}$	0.0369–0.0348	0.0374–0.0344	0.0422–0.0370
$u_{\tau M}$	0.0369–0.0348	0.0378–0.0351	0.0430–0.0378
u_τ	0.0369–0.0348	0.0376–0.0348	0.0427–0.0374
Re_τ	36.94–22.59	37.61–24.35	42.66–22.45

Table 3. Friction velocity (u_τ) and friction Reynolds number (Re_τ) for the three cases considered in the present study. $\overline{V_d}$ and $\overline{P_d}$ are viscous and pressure drags whereas the subscripts S and M refer to the stationary and moving walls, respectively. The symbols u_τ and Re_τ are also used to refer to the global friction velocity ($u_\tau = \sqrt{(u_{\tau S}^2 + u_{\tau M}^2)/2}$) and the corresponding global friction Reynolds number ($Re_\tau = u_\tau h/\nu$), respectively.

to calculate the friction velocity for the rough wall is the same as that of Mahmoodi-Jezeh & Wang (2020). When compared, the friction velocity u_τ at a particular Reynolds number is the highest in the k-type roughness. The enhanced friction in the k-type roughness promotes more turbulence generation compared with the d-type roughness and the smooth pCf, allowing it to sustain stable laminar–turbulent bands at lower Reynolds numbers than the other two cases. The values of u_τ for the d-type roughness closely resemble that of the smooth pCf, exhibiting only a marginal difference. Thereby, the d-type roughness seems to fail to induce greater turbulence generation compared with the smooth pCf.

Unlike the turbulent regime, $\bar{v}$ is not negligible in the transitional regime (see figure 15*b*). In the smooth pCf, the magnitude of $\bar{v}$ is zero at the stationary wall, increases to a negative peak and then drops to zero near the channel centre ($z = h$). At $z = h$, $\bar{v}$ changes sign, increases to a positive peak before falling to zero at the moving wall. The $\bar{v}$ variation in the rough pCf cases also exhibits a similar trend, except that, unlike the smooth pCf, the shift in sign occurs slightly away from the centre of the channel.

The mean wall-normal velocity $\bar{w}$ is not zero in the rough pCf cases as in the smooth pCf (see figure 15*c*). The $\bar{w}$ is non-zero near the ribs for the d-type roughness and becomes negligible beyond $z = 0.5h$. However, in the k-type roughness, $\bar{w}$ is predominantly non-zero and diminishes only close to the smooth-moving wall. In the d-type and the k-type roughness, $\bar{w}$ varies in the $-z$ direction at location I due to the fluid entering the cavities. At location II, $\bar{w}$ varies along the $+z$ direction for both the rough cases due to the upwards deflection of the flow near the rib crests. The $\bar{w}$ values in the d-type roughness are much smaller than its k-type counterpart as the effect of roughness on the outer flow is very limited in the former.

It is generally acknowledged that the secondary flow in the smooth pCf consists of counter-rotating secondary vortices (also known as roll cells) when the flow is turbulent. These vortices are critical in sustaining the elongated streaks in the turbulent flow (Hamilton *et al.* 1995). Javanappa & Narasimhamurthy (2021) were one of the first to report counter-rotating secondary vortices in rough turbulent Couette flows. Similarly, the secondary streamlines for the rough pCf cases in the present study reveal the presence of roll cells in the turbulent regime (see figure 16). Figure 17 shows the mean secondary flow streamlines for the rough pCf cases in the transitional regime. The counter-rotating vortices are not visible in the mean secondary flow. On the contrary, co-rotating vortices confined to the channel centre are observed. Examining the instantaneous fields is necessary before

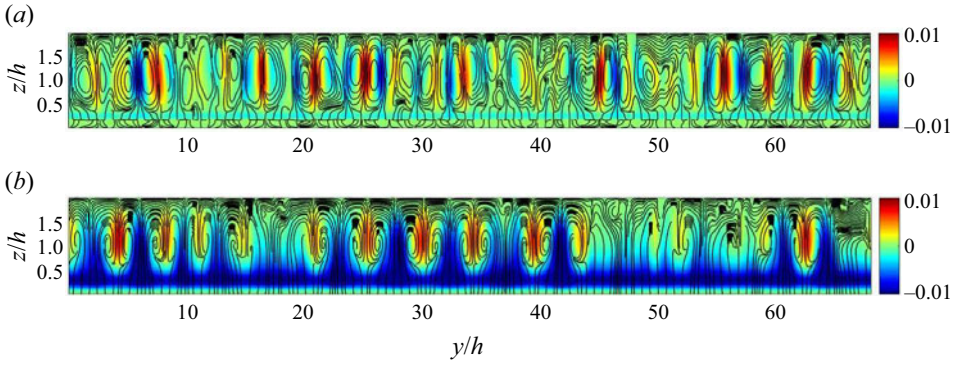

Figure 16. Mean secondary flow streamlines with mean wall-normal velocity in the background at $Re = 500$ for (*a*) d-type roughness and (*b*) k-type roughness at midcavity (I) location. The velocities used for generating streamlines and contours are averaged across time and pitches in the x direction.

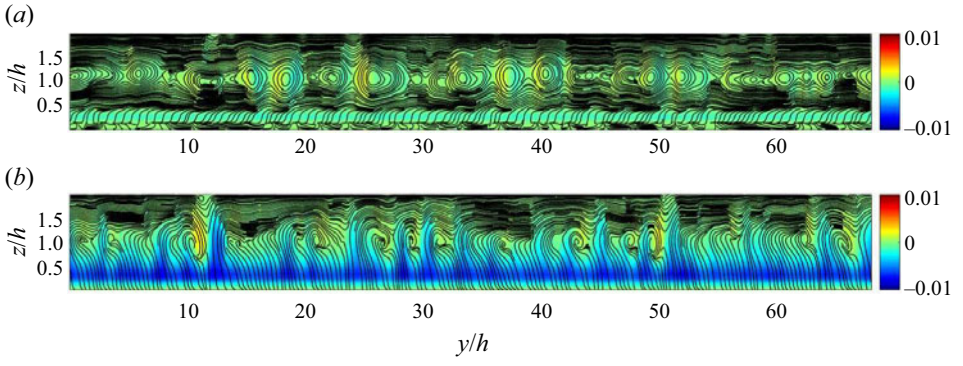

Figure 17. Mean secondary flow streamlines with mean wall-normal velocity in the background for (*a*) d-type roughness ($Re = 350$) and (*b*) k-type roughness ($Re = 300$) at midcavity (I) location. The velocities used for generating streamlines and contours are averaged across time and pitches in the x direction.

confirming the absence of the counter-rotating vortices in the transitional regime. Figure 18 shows the contours of instantaneous wall-normal velocity w for the d-type and the k-type roughness in a yz plane at $x/h = 0.1$ and $x/h = 0.9$, respectively. The changes in the direction of wall-normal velocity denote the existence of counter-rotating vortices in the turbulent region, while the laminar region exhibits an absence of such vortices. These vortices are directly connected to the elongated streaks in the turbulent bands. It is essential to note that the co-rotating vortices are not present in the instantaneous flow field. Therefore, the inference drawn is that the co-rotating vortices in figure 17 result from the averaging process, which includes the characteristics from both turbulent and quasi-laminar regions.

The Reynolds stresses for the rough pCf cases in the transitional regime are shown in figure 19. They are plotted at locations I and II, and the corresponding values in the smooth pCf are also presented. A comparison with the Reynolds stresses in the turbulent regime is also made to highlight the significant differences (see Appendix A for Reynolds stresses in the turbulent regime). In the d-type roughness, beyond $z = 0.5h$, the variations of Reynolds stresses are similar in shape to those in the smooth pCf. However, the curves for the d-type roughness and the smooth pCf never collapse on each other. The mismatch

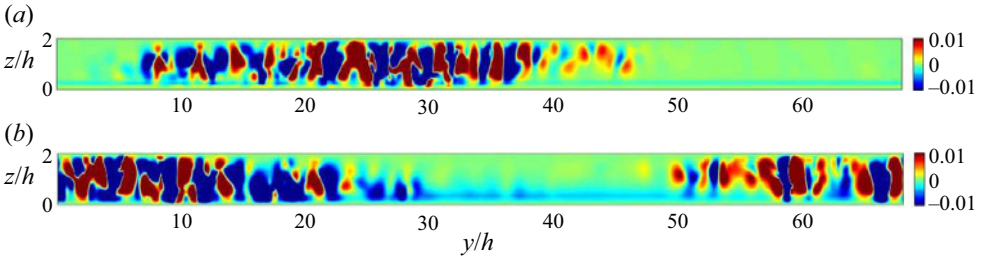

Figure 18. Instantaneous wall-normal velocity w for (a) d-type roughness ($Re = 350$) at $x/h = 0.1$ and (b) k-type roughness ($Re = 300$) at $x/h = 0.9$.

arises because the slope of the curves in the d-type roughness reaches zero at $z = 1.1h$ rather than at the midgap plane ($z = h$).

Unlike the d-type roughness, the Reynolds stress profiles in the k-type roughness are significantly different from those in the smooth pCf, especially in the bottom half of the channel. In addition, it is worth emphasising that the Reynolds stresses for the k-type roughness in the transitional and turbulent regimes have specific differences. The $\overline{u'u'}$ variation in the k-type roughness has a lower magnitude near the rib-roughened bottom wall compared with the smooth top wall when the flow is turbulent. Interestingly, in the transitional regime, this difference in the magnitude of the peaks in the bottom and top half of the channel diminishes. Similarly, the peak near the rib-roughened bottom wall for the $\overline{v'v'}$ variation at location II in the k-type roughness vanishes when the flow is in the transitional regime. However, there is still a sudden rise in the slope of the curve near the roughness crest, indicating a local intensification of spanwise fluctuations. The negative peak near the roughness crest for the $-\overline{u'w'}$ variation at location II in the k-type roughness is retained in the transitional regime.

We know that $-\overline{v'u'}$ and $-\overline{w'v'}$ are negligible when the flow is turbulent. In the transitional regime, these stress components are non-zero. It is worth noting that these off-diagonal stresses involving the spanwise velocity fluctuations (v') are non-zero in conjunction with a non-zero mean spanwise velocity ($\bar{v}$). The variations of $-\overline{v'u'}$ and $-\overline{w'v'}$ in the d-type and the k-type roughness are similar to that of the smooth pCf. Typically, in the rough pCf cases, $-\overline{v'u'}$ exhibits positive values, whereas $-\overline{w'v'}$ shows negative values. However, for the k-type roughness, there exists a small region corresponding to the cavity where $-\overline{v'u'}$ is marginally negative, and $-\overline{w'v'}$ is marginally positive. The Reynolds stress profiles at locations I and II collapse beyond $z = 0.5h$ for the d-type roughness. In the k-type roughness, the profiles at I and II merge beyond $z = h$ except for the variation of $-\overline{w'v'}$, where the curves collapse close to the smooth moving wall.

The Reynolds stresses presented in the present study have contributions from the turbulent and the quasi-laminar regions. However, estimating Reynolds stresses for the turbulent and the laminar bands separately can be challenging. Instead, we perform a spatial average of the product of velocity fluctuations ($u_i'u_j'$) along the bands (x_d direction) at an instant and estimate the relative contributions. Here, we show $u'u'$ data from the rough pCf cases to demonstrate this averaging process, which can be appropriately called diagonal averaging. Figure 20 shows the contours of $u'u'$ in an x–y plane at the midgap location (note that the flow domain is replicated in the y direction to obtain an extended view). The diagonal averaging is performed in the x_d direction ($(1/L)\int u'u'\,\mathrm{d}x_d$, where L

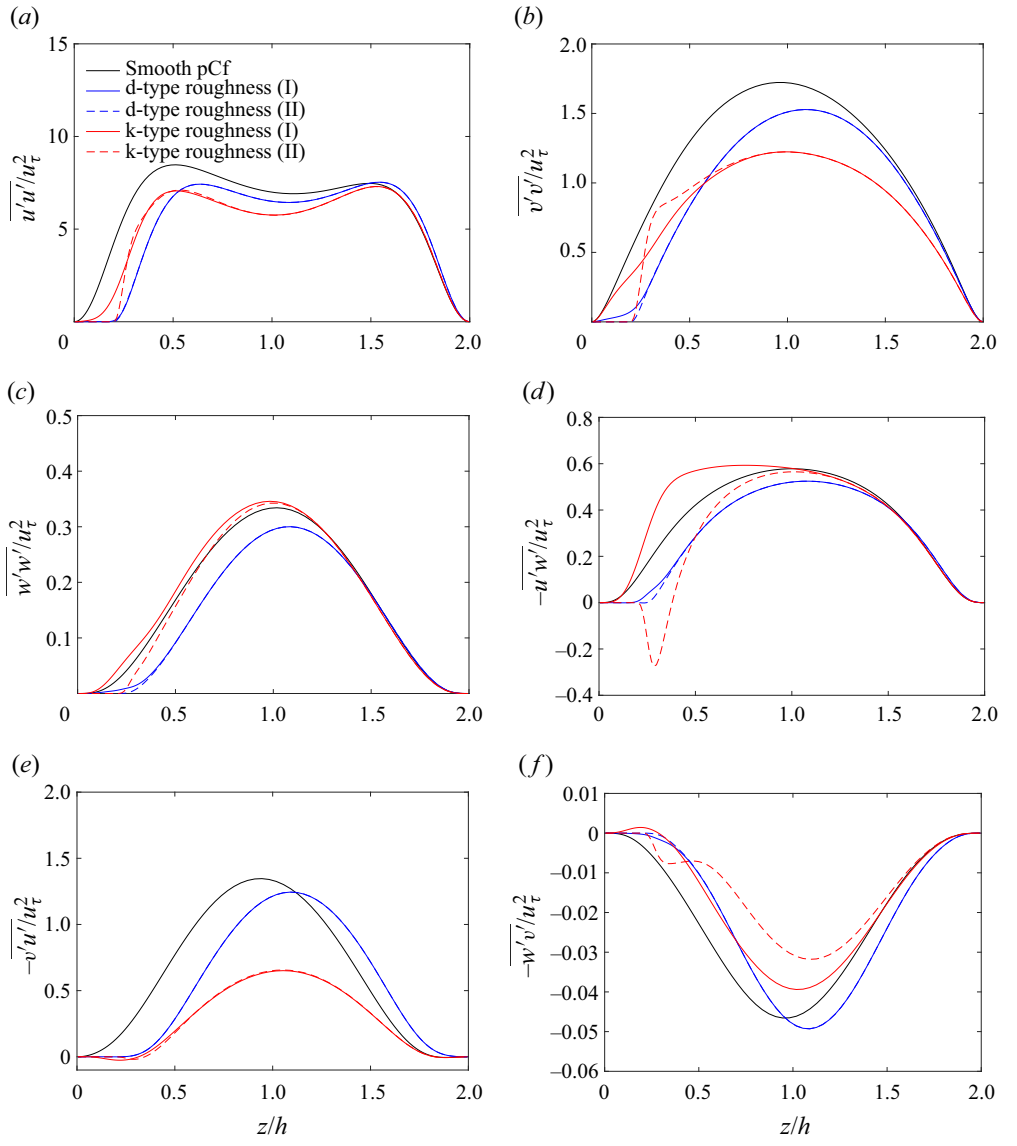

Figure 19. Variation of components of Reynolds stress tensor (*a–f*) along the wall-normal direction for d-type roughness and k-type roughness at the midcavity (I) and midrib (II) locations at a Reynolds number close to their Re_g. Corresponding Reynolds stresses in smooth pCf are also plotted for comparison. The stresses are normalised using the square of global friction velocity u_τ^2 of each case.

is the diagonal length) for a laminar–turbulent band (shown within the tilted rectangular box) at all x–y planes in the domain. The diagonally averaged $\langle u'u'\rangle_d$ in the y–z plane for the turbulent and the quasi-laminar regions is shown in figure 21. Further, the data are averaged along the y direction for the turbulent and the quasi-laminar regions. This allows us to obtain the wall-normal variation of $\langle u'u'\rangle_d$ for each distinct region (see figure 22). In the quasi-laminar region, the contribution to $\langle u'u'\rangle_d$ is significant due to the non-zero streamwise velocity fluctuations, unlike in the laminar Couette flow. However, the magnitudes are smaller compared with those from the turbulent region. Despite the

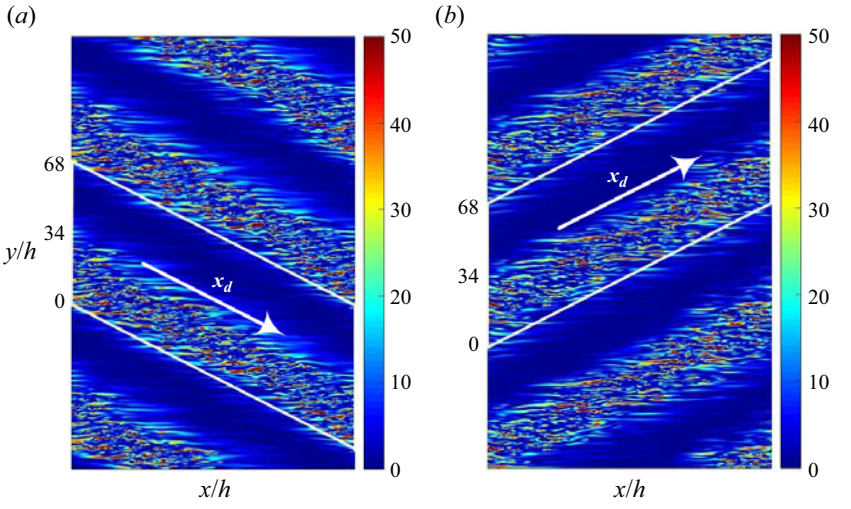

Figure 20. Contours of $u'u'$ at the midgap location ($z = h$) for (*a*) d-type roughness ($Re = 350$) and (*b*) k-type roughness ($Re = 300$). The product of streamwise velocity fluctuations is normalised by u_τ^2 of each case.

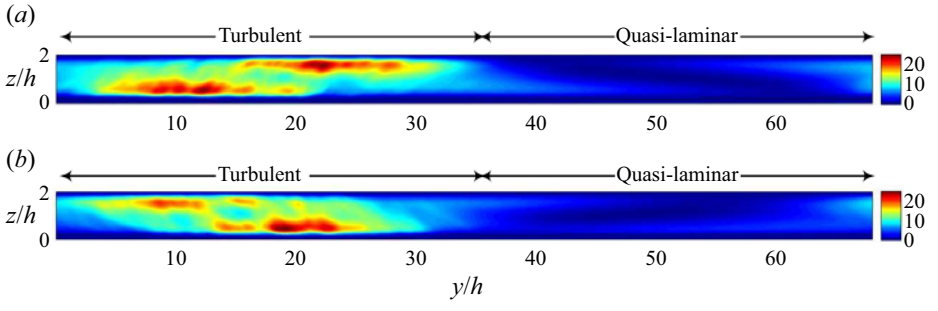

Figure 21. Diagonally averaged $\langle u'u' \rangle_d$ in the y–z plane for (*a*) d-type roughness ($Re = 350$) and (*b*) k-type roughness ($Re = 300$). The data are normalised by u_τ^2 of each case. Note that $\langle\ \rangle_d$ represents spatial averaging along the bands (diagonal).

significant difference in the magnitudes, the curves of $\langle u'u' \rangle_d$ for both regions exhibit a similar trend. The combined average of $\langle u'u' \rangle_d$, with the contributions from both the turbulent and the quasi-laminar regions, is reasonably closer to the variation of Reynolds stress $\overline{u'u'}$ at the midcavity (I) location. Diagonal averaging can also be performed on the remaining $u_i'u_j'$ components to get the corresponding turbulent and quasi-laminar contributions (see figure 26 in Appendix A for the wall-normal variations of all $\langle u'u' \rangle_d$ components in the turbulent and the quasi-laminar regions for the rough pCf cases).

4. Conclusions

DNS have been performed to study the effect of roughness on the transition to turbulence in pCf. Two rough pCf cases are considered, with pitch separations $\lambda = 2k$ and $\lambda = 10k$, which fall in the d-type and the k-type roughness category, respectively. Reynolds number is reduced gradually in steps to achieve a reverse transition. Smooth pCf is known to have stable laminar–turbulent bands for $Re \in [325, 400]$. Similar to the smooth pCf, a stage of oblique laminar–turbulent bands is found in both the d-type and the k-type roughness

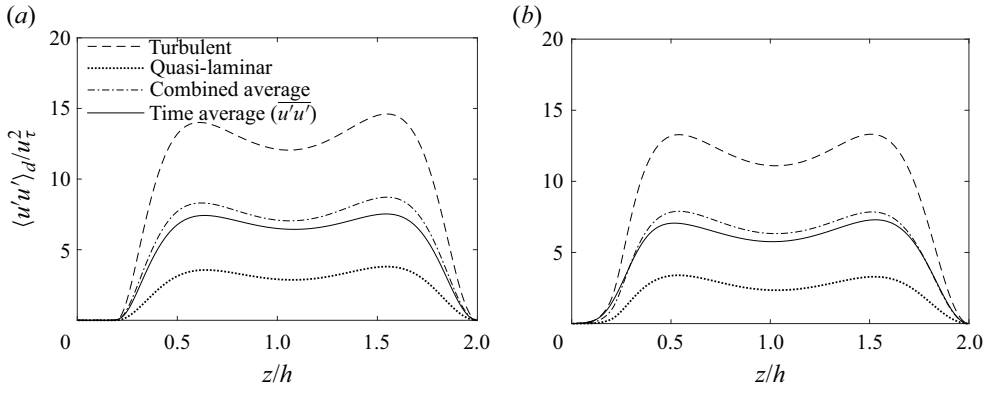

Figure 22. Wall-normal variation of $\langle u'u'\rangle_d$ for (*a*) d-type roughness ($Re = 350$) and (*b*) k-type roughness ($Re = 300$). The variation of Reynolds stress $\overline{u'u'}$ (obtained using time averaging) at the midcavity (I) location is also presented for comparison. Profiles are normalised by u_τ^2 of each case.

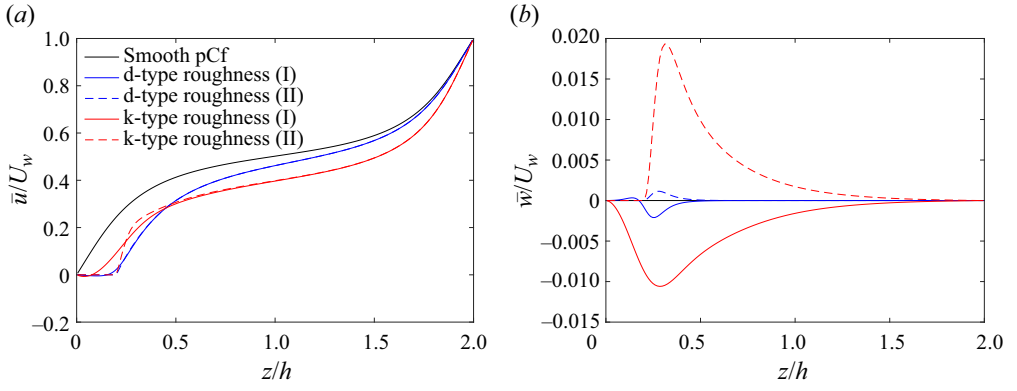

Figure 23. Variation of (*a*) mean streamwise velocity $\bar{u}$ and (*b*) mean wall-normal velocity $\bar{w}$ along the wall-normal direction for d-type roughness and k-type roughness at the midcavity (I) and midrib (II) locations at $Re = 500$. Velocity profiles in smooth pCf ($Re = 500$) is also plotted for comparison. Mean spanwise velocity $\bar{v}$ is negligible for all the cases.

in the transitional regime. In the k-type roughness, stable laminar–turbulent bands are observed for the Reynolds numbers in the range $Re \in [300, 325]$. The transitional range has narrowed and has shifted to lower Reynolds numbers compared with the smooth pCf. The ribs of the k-type roughness can act as vortex generators and aid the regeneration of vorticity so that the oblique bands are sustained at lower Reynolds numbers as opposed to the smooth pCf. However, the transitional range in the d-type roughness ($Re \in [350, 425]$) has shifted upwards compared with the smooth pCf. This peculiar behaviour is most likely due to the inherent lack of ability of the d-type roughness to effectively shed vortices into the outer flow and, thus, its negligible contribution to vorticity regeneration. Moreover, the streamwise-elongated structures in the d-type roughness are located further away from the wall, indicating a relatively stable zone in the near-wall region that could potentially inhibit streak formation. Previous studies on d-type roughness with a pitch separation of $\lambda = 2k$ (e.g. Leonardi *et al.* 2004, 2007; MacDonald *et al.* 2018) have not reported a significant difference in the near-wall streaks between the d-type roughness and the smooth case, except for a reduction in their length. However, these studies were conducted in channel

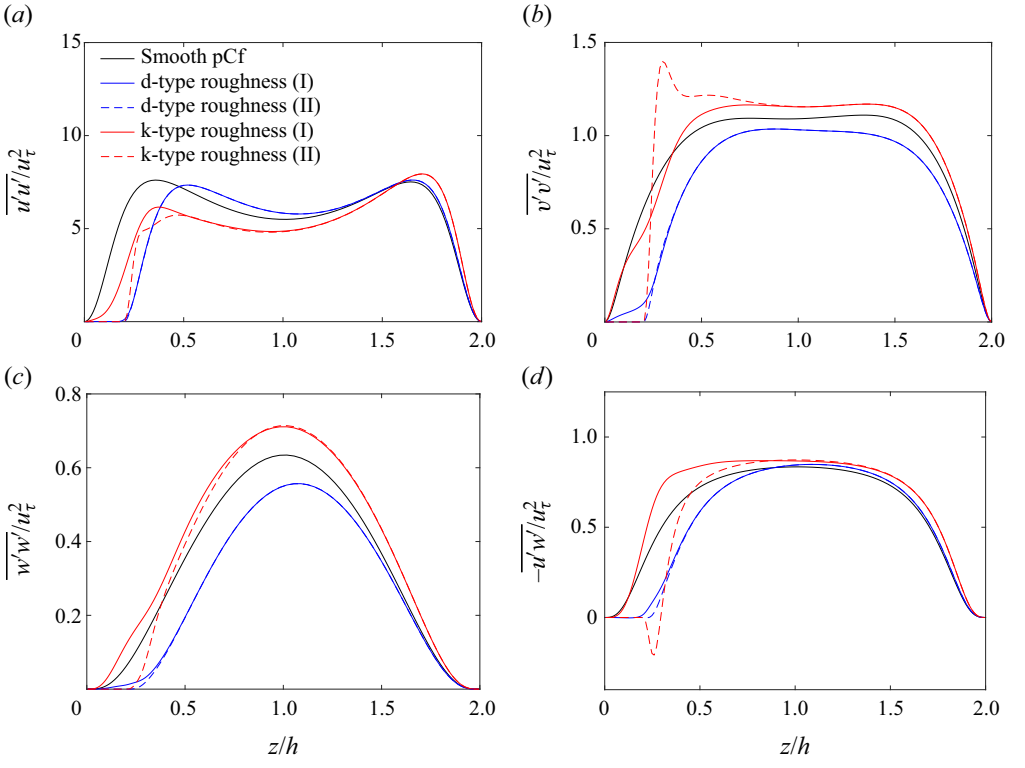

Figure 24. Variation of components of Reynolds stress tensor along the wall-normal direction for d-type roughness and k-type roughness at the midcavity (I) and midrib (II) locations at $Re = 500$. Reynolds stresses in smooth pCf ($Re = 500$) are also plotted for comparison. Here $-\overline{v'u'}$ and $-\overline{w'v'}$ are negligible for all the cases. The stresses are normalised using the square of global friction velocity u_τ^2 of each case.

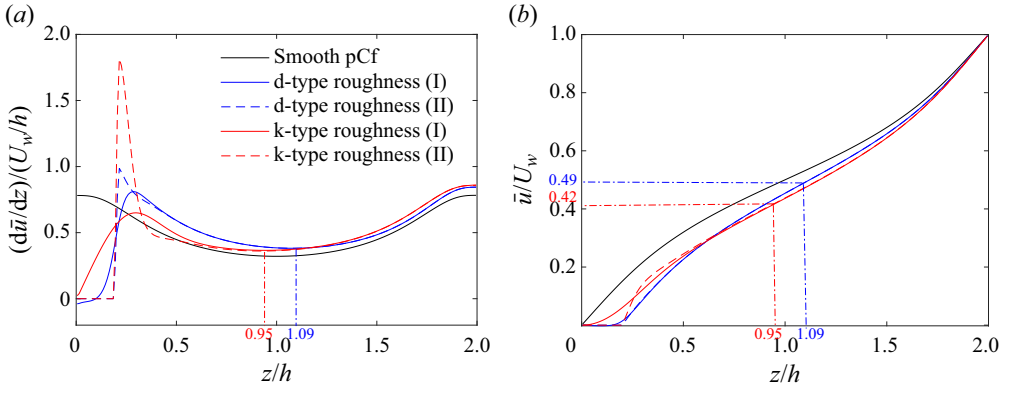

Figure 25. Variation of (*a*) mean velocity gradient $\mathrm{d}\bar{u}/\mathrm{d}z$ and (*b*) mean streamwise velocity $\bar{u}$ along the wall-normal direction for d-type roughness and k-type roughness at the midcavity (I) and midrib (II) locations at a Reynolds number close to their Re_g. Corresponding profiles in smooth pCf are also plotted for comparison.

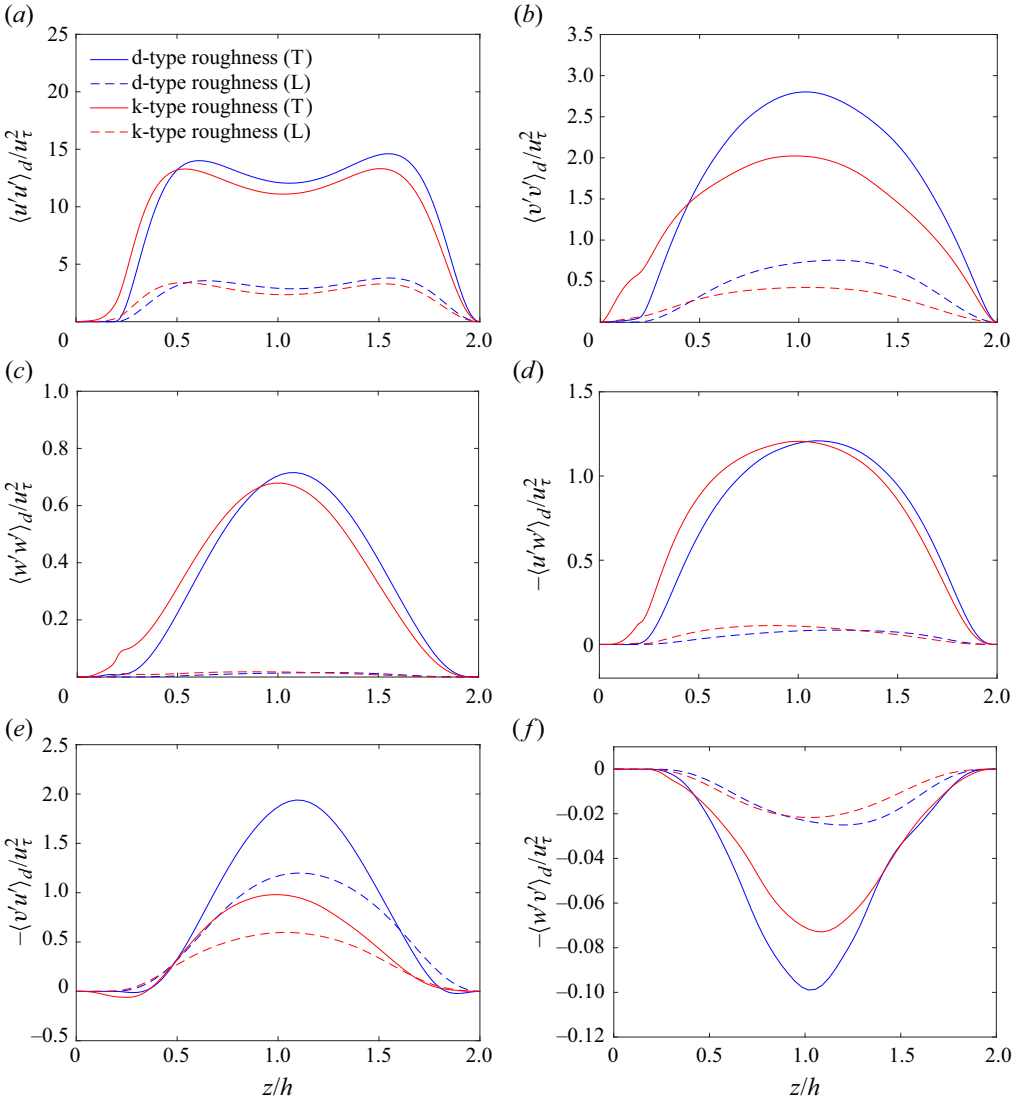

Figure 26. Wall-normal variation of $\langle u_i' u_j' \rangle_d$ for the rough pCf cases at a Reynolds number close to their Re_g. The values are normalised using u_τ^2 of each case. The legend labels (T) and (L) indicate the turbulent and quasi-laminar regions, respectively.

flows at Reynolds numbers that are higher than those in the present study, which focuses on the characteristics of rough Couette flows within the transitional flow regime.

The large-scale flow in the rough pCf cases is parallel to the oblique bands near the laminar–turbulent boundaries, indicative of a significant spanwise velocity component. The peak of the probability density function of the angle made by the large-scale flow vectors gives the most likely orientation of the large-scale flow. As a major portion of the flow is parallel to the oblique bands, the most likely angle matches well with the corresponding pattern angle. Similar to the spatial planes, spatiotemporal diagrams reveal laminar–turbulent coexistence as oblique bands. The frequency/time period of the patterns in the rough pCf cases is found using an FFT technique. The pattern in the d-type

roughness has about four cycles in $1000h/U_w$, and its k-type counterpart has approximately three cycles every $1000h/U_w$. The frequency/time period remains the same regardless of the Reynolds number.

The secondary flow in the transitional regime shows the presence of counter-rotating vortices in the turbulent regions. These vortices are integral in maintaining the elongated streaks which constitute the turbulent bands. The main effect of having a non-zero spanwise velocity is reflected in the off-diagonal components of the Reynolds stress tensor. The gradient $\partial\bar{v}/\partial z$ in the production term of the Reynolds stresses $-\overline{v'u'}$ and $-\overline{w'v'}$ does not approach zero, leading to non-zero production. $-\overline{v'u'}$ and $-\overline{w'v'}$, which were zero in the turbulent regime, are now non-zero and, thus, relevant.

The results from the present study can be compared with those of Ishida *et al.* (2017). Both studies concur that the transition to turbulence occurs through a stage of alternate laminar–turbulent bands when the roughness height is $k = 0.2h$. Their model predicts a rise in the friction Reynolds number due to roughness, and this observation aligns with the behaviour of the k-type roughness employed in the present study. Apart from these points, a direct quantitative comparison is challenging as the present roughness pitch analogous to the roughness density used in their parametric model is difficult to determine. We anticipate that forthcoming research will further substantiate our findings. We also believe that this study provides a foundational understanding of the effects of roughness on the transition to turbulence in pCf. It can be extended to investigate the effect of roughness by altering the shape, height, dimensionality and arrangement of the roughness. Configurations such as longitudinal roughness, oblique roughness and incoherent random roughness can also be considered.

Funding. This work is financially supported by the Science and Engineering Research Board (SERB), Department of Science and Technology, Government of India (Core Research Grant No. CRG/2018/004926).

Declaration of interests. The authors report no conflict of interest.

Author ORCIDs.
Vagesh D. Narasimhamurthy https://orcid.org/0000-0002-1759-3186.

Appendix A

A.1. *Mean quantities at Re = 500*

Figures 23 and 24 show the mean quantities at $Re = 500$.

A.2. *Apparent midgap*

The apparent midgap is located at the minimum of $\mathrm{d}\bar{u}/\mathrm{d}z$ above the roughness layer (Ishida *et al.* 2017). The apparent midgaps and the corresponding mean streamwise velocities for the rough pCf cases are marked in figure 25.

A.3. *Turbulent and quasi-laminar components of* $\langle u_i' u_j' \rangle_d$

The turbulent and quasi-laminar components of $\langle u_i' u_j' \rangle_d$ are plotted in figure 26.

References

Ashrafian, A., Andersson, H.I. & Manhart, M. 2004 DNS of turbulent flow in a rod-roughened channel. *Intl J. Heat Fluid Flow* **25** (3), 373–383.

AVILA, K., MOXEY, D., DE LOZAR, A., AVILA, M., BARKLEY, D. & HOF, B. 2011 The onset of turbulence in pipe flow. *Science* **333** (6039), 192–196.
AVILA, M., BARKLEY, D. & HOF, B. 2023 Transition to turbulence in pipe flow. *Annu. Rev. Fluid Mech.* **55**, 575–602.
AYDIN, E. & LEUTHEUSSER, H. 1991 Plane-Couette flow between smooth and rough walls. *Exp. Fluids* **11** (5), 302–312.
AYDIN, M. & LEUTHEUSSER, H.J. 1979 Novel experimental facility for the study of plane Couette flow. *Rev. Sci. Instrum.* **50** (11), 1362–1366.
BARKLEY, D. & TUCKERMAN, L.S. 2005 Computational study of turbulent laminar patterns in Couette flow. *Phys. Rev. Lett.* **94** (1), 014502.
BARKLEY, D. & TUCKERMAN, L.S. 2007 Mean flow of turbulent–laminar patterns in plane Couette flow. *J. Fluid Mech.* **576**, 109–137.
BECH, K.H., TILLMARK, N., ALFREDSSON, P.H. & ANDERSSON, H.I. 1995 An investigation of turbulent plane Couette flow at low Reynolds numbers. *J. Fluid Mech.* **286**, 291–325.
BOTTIN, S. & CHATÉ, H. 1998 Statistical analysis of the transition to turbulence in plane Couette flow. *Eur. Phys. J.* B *Condens. Matt. Complex Syst.* **6**, 143–155.
BUSSE, A. & SANDHAM, N.D. 2012 Parametric forcing approach to rough-wall turbulent channel flow. *J. Fluid Mech.* **712**, 169–202.
CHOI, K.S. & FUJISAWA, N. 1993 Possibility of drag reduction using d-type roughness. *Appl. Sci. Res.* **50**, 315–324.
COLEMAN, S., NIKORA, V.I., MCLEAN, S. & SCHLICKE, E. 2007 Spatially averaged turbulent flow over square ribs. *J. Engng Mech.* **133** (2), 194–204.
CUI, J., PATEL, V.C. & LIN, C.-L. 2003 Large-eddy simulation of turbulent flow in a channel with rib roughness. *Intl J. Heat Fluid Flow* **24** (3), 372–388.
DAVIAUD, F., HEGSETH, J. & BERGÉ, P. 1992 Subcritical transition to turbulence in plane Couette flow. *Phys. Rev. Lett.* **69** (17), 2511.
DUGUET, Y. & SCHLATTER, P. 2013 Oblique laminar-turbulent interfaces in plane shear flows. *Phys. Rev. Lett.* **110** (3), 034502.
DUGUET, Y., SCHLATTER, P. & HENNINGSON, D.S. 2010 Formation of turbulent patterns near the onset of transition in plane Couette flow. *J. Fluid Mech.* **650**, 119–129.
EL TELBANY, M. & REYNOLDS, A. 1980 Velocity distributions in plane turbulent channel flows. *J. Fluid Mech.* **100** (1), 1–29.
EL TELBANY, M. & REYNOLDS, A. 1981 Turbulence in plane channel flows. *J. Fluid Mech.* **111**, 283–318.
GOKUL, S. & NARASIMHAMURTHY, V.D. 2022 Characteristics of transitional plane Couette flow. *Intl J. Fluid Mech. Res.* **49** (3), 19–30.
GOMÉ, S., TUCKERMAN, L.S. & BARKLEY, D. 2023*a* Patterns in transitional shear turbulence. Part 1. Energy transfer and mean-flow interaction. *J. Fluid Mech.* **964**, A16.
GOMÉ, S., TUCKERMAN, L.S. & BARKLEY, D. 2023*b* Patterns in transitional shear turbulence. Part 2. Emergence and optimal wavelength. *J. Fluid Mech.* **964**, A17.
GRÖTZBACH, G. 1983 Spatial resolution requirements for direct numerical simulation of the Rayleigh–Bénard convection. *J. Comput. Phys.* **49** (2), 241–264.
HAMILTON, J.M., KIM, J. & WALEFFE, F. 1995 Regeneration mechanisms of near-wall turbulence structures. *J. Fluid Mech.* **287**, 317–348.
HOF, B., WESTERWEEL, J., SCHNEIDER, T.M. & ECKHARDT, B. 2006 Finite lifetime of turbulence in shear flows. *Nature* **443** (7107), 59–62.
HOLSTAD, A., ANDERSSON, H.I. & PETTERSEN, B. 2010 Turbulence in a three-dimensional wall-bounded shear flow. *Intl J. Numer. Meth. Fluids* **62** (8), 875–905.
HU, Z., MORFEY, C.L. & SANDHAM, N.D. 2003 Sound radiation in turbulent channel flows. *J. Fluid Mech.* **475**, 269–302.
ISHIDA, T., BRETHOUWER, G., DUGUET, Y. & TSUKAHARA, T. 2017 Laminar-turbulent patterns with rough walls. *Phys. Rev. Fluids* **2** (7), 073901.
ISHIDA, T., DUGUET, Y. & TSUKAHARA, T. 2017 Turbulent bifurcations in intermittent shear flows: from puffs to oblique stripes. *Phys. Rev. Fluids* **2** (7), 073902.
JAVANAPPA, S.K. & NARASIMHAMURTHY, V.D. 2020 DNS of plane Couette flow with surface roughness. *Intl J. Adv. Engng Sci. Appl. Math.* **11** (4), 288–300.
JAVANAPPA, S.K. & NARASIMHAMURTHY, V.D. 2021 Turbulent plane Couette flow with a roughened wall. *Phys. Rev. Fluids* **6** (10), 104609.
JAVANAPPA, S.K. & NARASIMHAMURTHY, V.D. 2022 Structure of turbulence in planar rough Couette flows. *Phys. Fluids* **34** (6), 065124.

JEONG, J. & HUSSAIN, F. 1995 On the identification of a vortex. *J. Fluid Mech.* **285**, 69–94.
JIMÉNEZ, J. 2004 Turbulent flows over rough walls. *Annu. Rev. Fluid Mech.* **36**, 173–196.
KASHYAP, P.V., DUGUET, Y. & DAUCHOT, O. 2022 Linear instability of turbulent channel flow. *Phys. Rev. Lett.* **129** (24), 244501.
KOLMOGOROV, A.N. 1941 The local structure of turbulence in incompressible viscous fluid for very large Reynolds numbers. *C. R. Acad. Sci. URSS* **30**, 301–305.
KRISTOFFERSEN, R., BECH, K.H. & ANDERSSON, H.I. 1993 Numerical study of turbulent plane Couette flow at low Reynolds number. In *Advances in Turbulence IV*, pp. 337–343. Springer.
LEE, M.J. & KIM, J. 1991 The structure of turbulence in a simulated plane Couette flow. In *Proceedings of the 8th Symposium on Turbulent Shear Flow*, vol. 1, pp. 531–536. Technical University of Munich.
LEONARDI, S., ORLANDI, P. & ANTONIA, R.A. 2007 Properties of d- and k-type roughness in a turbulent channel flow. *Phys. Fluids* **19** (12), 125101.
LEONARDI, S., ORLANDI, P., DJENIDI, L. & ANTONIA, R.A. 2004 Structure of turbulent channel flow with square bars on one wall. *Intl J. Heat Fluid Flow* **25** (3), 384–392.
LUCHINI, P., MANZO, F. & POZZI, A. 1991 Resistance of a grooved surface to parallel flow and cross-flow. *J. Fluid Mech.* **228**, 87–109.
MACDONALD, M., OOI, A., GARCÍA-MAYORAL, R., HUTCHINS, N. & CHUNG, D. 2018 Direct numerical simulation of high aspect ratio spanwise-aligned bars. *J. Fluid Mech.* **843**, 126–155.
MAHMOODI-JEZEH, S. & WANG, B.-C. 2020 Direct numerical simulation of turbulent flow through a ribbed square duct. *J. Fluid Mech.* **900**, A18.
MALERUD, S., MÀLO/Y, K.J. & GOLDBURG, W.I. 1995 Measurements of turbulent velocity fluctuations in a planar Couette cell. *Phys. Fluids* **7** (8), 1949–1955.
MANHART, M. 2004 A zonal grid algorithm for DNS of turbulent boundary layers. *Comput. Fluids* **33** (3), 435–461.
MANNEVILLE, P. 2011 On the decay of turbulence in plane Couette flow. *Fluid Dyn. Res.* **43** (6), 065501.
MANNEVILLE, P. & ROLLAND, J. 2011 On modelling transitional turbulent flows using under-resolved direct numerical simulations: the case of plane Couette flow. *Theor. Comput. Fluid Dyn.* **25** (6), 407–420.
NAGANO, Y., HATTORI, H. & HOURA, T. 2004 DNS of velocity and thermal fields in turbulent channel flow with transverse-rib roughness. *Intl J. Heat Fluid Flow* **25** (3), 393–403.
NIKURADSE, J. 1933 Laws for flow in rough pipes. *NASA Tech. Rep.* NACA TM 1292, 1950. *English translation of VDI-Forschungsheft* 361.
PERRY, A.E., SCHOFIELD, W.H. & JOUBERT, P.N. 1969 Rough wall turbulent boundary layers. *J. Fluid Mech.* **37** (2), 383–413.
PHILIP, J. & MANNEVILLE, P. 2011 From temporal to spatiotemporal dynamics in transitional plane Couette flow. *Phys. Rev.* E **83** (3), 036308.
PRIGENT, A., GRÉGOIRE, G., CHATÉ, H. & DAUCHOT, O. 2003 Long-wavelength modulation of turbulent shear flows. *Phys.* D*: Nonlinear Phenom.* **174** (1-4), 100–113.
TILLMARK, N. & ALFREDSSON, P.H. 1992 Experiments on transition in plane Couette flow. *J. Fluid Mech.* **235**, 89–102.
TOWNSEND, A.A. 1976 *The Structure of Turbulent Shear Flow*, 2nd edn. Cambridge University Press.
TSUKAHARA, T., KAWAGUCHI, Y. & KAWAMURA, H 2009 DNS of turbulent plane Couette flow with emphasis on turbulent stripe. In *Advances in Turbulence XII*, pp. 71–74. Springer.
TSUKAHARA, T., TOMIOKA, T., ISHIDA, T., DUGUET, Y. & BRETHOUWER, G. 2018 Transverse turbulent bands in rough plane Couette flow. *J. Fluid Sci. Technol.* **13** (3), 1–19.